# Studies on composite biomaterials
## PhD thesis summary

Faculty of Physics

PhD Student:

**Adriana Vulpoi**

Scientific Supervisor:

Prof. Dr. Viorica Simon

**2011**

# Contents

# 1 INTRODUCTION

The aim of this thesis is to synthesise composite biomaterials for further possible tissue engineering purposes. Tissue engineering is an interdisciplinary field that applies the principles of life science and engineering to the development of biological substitutes that aim to maintain, restore or improve tissue function. Biodegradable materials have found enormous interest as supports because of the fact that the support disappears from the transplantation site with the passage of time, leaving behind a perfect patch of the natural tissue. Therefore this thesis is based on preparation and characterization of bioactive, biodegradable and antibacterial polymer/ bioactive glass composites.

The bioactive property of the chosen composite is given by bioactive glass in the formula $56SiO_2 \cdot (40-x)CaO \cdot 4P_2O_5 \cdot xAg_2O$ with x = 0, 2, 4, 6, 8 and 10 mol%. The preparation method chosen for these bioactive glasses is sol-gel method because it permits a low temperature preparation and a better controllability of the bioactive glass structure and morphology. This method also permitted the introduction of the antibacterial agent in the glass composition giving these samples a composite nature with metallic silver as dispersed phase in an almost amorphous glass structure.

The biodedegradable component is given by a Poly-96L/4 D-lactide copolymer highly porous structures. A slurry-dipping technique was use to obtain the polymer/silver-bioactive glass composites.

This thesis begins with the present introduction followed by four chapters and finishes with conclusions. Each chapter is followed by references.

The introduction presents the motivation and the main objective of this thesis. The first chapter of this thesis is dedicated to Biomaterials, beginning with a general definition of these materials and trying to overview this vast domain, focusing on bioactive glasses, polymers and their composites, as biomaterials. The second chapter contains brief descriptions of the experimental techniques used for analysis of the samples. In the third chapter are described the experimental proceedings for both preparing and analyzing the samples. In the last chapter are presented the experimental results and also discussions on their behalf.

# 2 SILVER-BIOACTIVE GLASS COMPOSITES

One of the aims of this study was to evaluate the nature of the silver species embedded into the bioactive glass network before and after immersion in simulated body fluid (SBF), and to characterize the structural, morphological and textural changes induced by the silver addition to the bioactive glass matrix. Special attention was also focused on determining how silver content influences the bioactivity of the investigated glasses and to investigate the protein binding capability of the Ag containing bioactive glasses.

## 2.1 Materials and samples preparation

Samples belonging to the system $56SiO_2 \cdot (40-x)CaO \cdot 4P_2O_5 \cdot xAg_2O$ with x = 0, 2, 4, 6, 8 and 10 mol% were prepared via sol-gel method. The gels were obtained by hydrolysis and condensation of tetraethyl orthosilicate (TEOS), calcium nitrate tetrahydrate ($Ca(NO_3)_2 \cdot 4H_2O$) ammonium phosphate dibasic (($NH_4)_2HPO_4$) and silver nitrate ($AgNO_3$).

First the bioactive glass matrix belonging to the composition $56SiO_2 \cdot 40CaO \cdot 4P_2O_5$ was prepared. It was further denoted the sample with x=0. For this reason TEOS was mixed with ethanol in a weight ratio of 1:1 and kept on a magnetic stirrer at room temperature for an hour. In this time $Ca_2O$ and $P_2O_5$ precursors were dissolved in distillated water separately and left on magnetic stirrers for 30 minutes also at room temperature. After one hour the three clear solutions were mixed together. First the calcium containing solution was added drop by drop to the TEOS solution under continuous stirring. After that the phosphor containing solution has been added also drop by drop under continuous stirring. The pH of the final solution was adjusted to 1.5 with nitric acid ($HNO_3$), and left on the magnetic stirrer for other two hours. After removing from the stirrer the samples the pot containing the solution was transferred to an incubator and kept there for seven days in order to obtain the gel, respectively aging. The aged gel was placed on a watch glass dried in an oven at 110 ºC for 24 hours in order to eliminate water excess and the alcohol obtained from the hydrolysis..

The silver containing samples were prepared similar with the silver free sample. This samples were named x=2, x=4, x=6, x=8 and x=10 respectively closely related with the silver concentration added. $Ag_2O$ was introduced by partially substitution of CaO. The $Ag_2O$ precursor was also dissolved in distillated water but this time the pH of the solution was adjusted to 2 with

nitric acid to avoid precipitation. In this case the first solution added on the TEOS solution was the silver containing one. The rest of the preparation protocol was the same with the one of the silver free sample.

After drying, all the samples were well grounded and were heat treated at 580°C for 1/2h. The samples were introduced in the preheated oven and taken out after 30 minutes.

## 2.2   Characterization of the prepared sol-gel glasses

DTA and TGA were used to understand how the silver presence influences the thermal events, while XRD, FTIR spectroscopy were applied to determine both the developed crystalline phases and the structural changes generated inside the matrix by the addition of such high amount of silver. The textural particularities of the investigated samples are proposed to be determined by performing $N_2$-adsorption measurements. The shape and size distribution of the silver particles located inside the glass matrix were studied by TEM, UV-vis

### 2.2.1   DTA/TG

The TGA/DTA curves of the as prepared samples are shown in Fig. 1. The first endothermic peak located around 60-80 ℃ and associated with the weight loss can be observed in all investigated samples and corresponds to the release of physisorbed water and the pore liquor [1]. The exothermic peak with an onset around 277 ℃ could be assigned to the removal of organic residues. A relative intense endothermic signal appears in the DTA curves around 485 ℃ for the samples with x=4 and x=6 and could be associated with the silver oxide decomposition and possibly metallic silver nanocrystals formation. Its presence for higher silver content (x=8 and x=10) cannot be excluded as long as the peak located around 500 ℃ becomes more pronounced and cover the temperature range near 485 ℃.
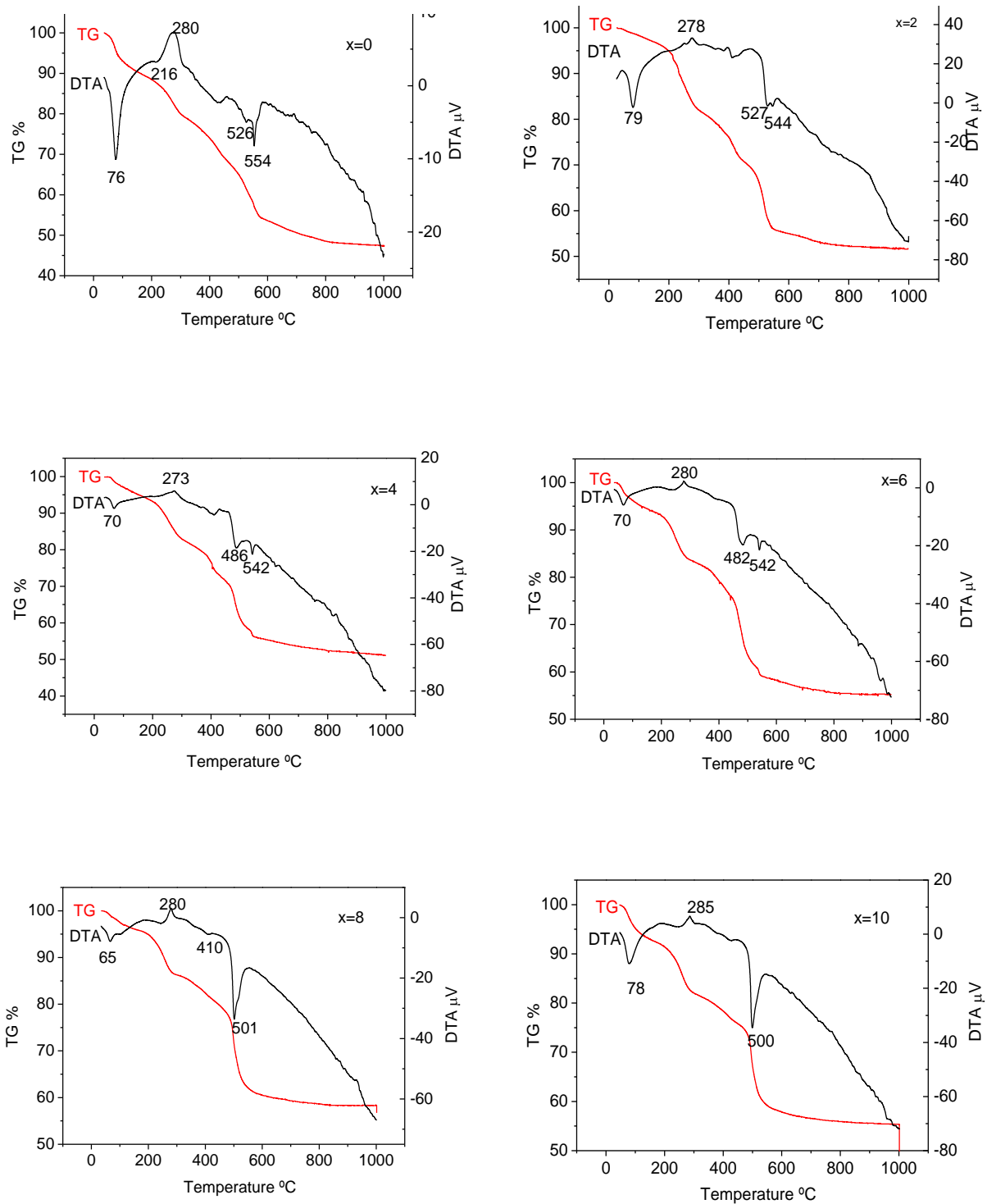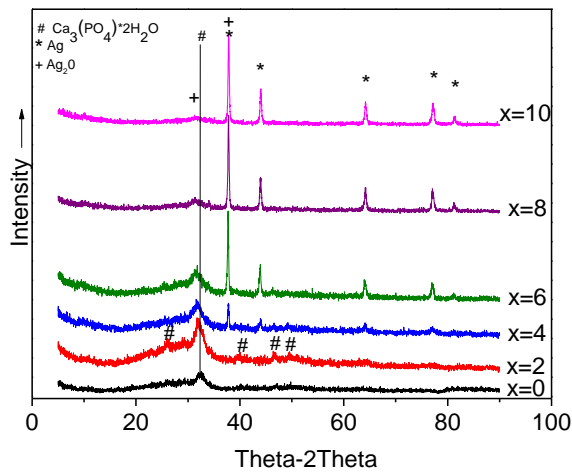
**Fig. 1** TG/DTA curves of the $56SiO_2 \cdot (40-x)CaO \cdot 4P_2O_5 \cdot xAg_2O$ samples. Note that the DTA curve is represented by the top line, while the bottom line represents the TG signal.

The endothermic peaks from the 540-550 ℃ temperature range, which occur for the samples with $0 \leq x \leq 6$, are mainly due dehidroxylation and are associated with the weight loss from the corresponding TGA curves [2]. The thermal events corresponding to the metallic silver nanocrystals formation and dehidroxilation are overlaid with the silver addition (x=8 and x=10) and lead to a maximum around 500 ℃. A close analysis of the endothermic peaks position between 540 and 550 ℃ reveals the decrease of the temperature, where the thermal event takes place, as silver content increases.

### 2.2.2  XRD

The XRD patterns of the investigated samples displayed in Fig. 2 exhibit mainly amorphous characteristics corresponding to glass, but they show incipient crystallization of a tricalcium phosphate (TCP) phase identified as $Ca_3(PO_4)_2$·centered at $2\theta=32°$ [1, 2].



**Fig. 4.3**  XRD patterns of the $56SiO_2 \cdot (40-x)CaO \cdot 4P_2O_5 \cdot xAg_2O$ samples

This result suggests that the incorporation of such a high amount of silver into the investigated $SiO_2$-CaO-$P_2O_5$ system does not compromise its bioactivity. XRD patterns of the samples with $x \geq 4$ mol % shows their composites nature with metallic silver as dispersed phase, but also an $Ag_2O$ phase consisting of very small crystallites that is less visible as silver content increases. This is in agreement with the above mentioned assumption from DTA analysis concerning the endothermic event located around 485 ℃ that was associated with the metallic

silver nanocrystals formation. One also observes that the increase of the silver content causes an expected increase of crystallized metallic silver amount.

### 2.2.3   IR

The IR spectra presented in Fig. 3 show the existence of $Q_4$ units (1200-1260 cm$^{-1}$) in all samples. No other significant change can be observed in the IR spectra of the investigated silver containing bioactive glasses.
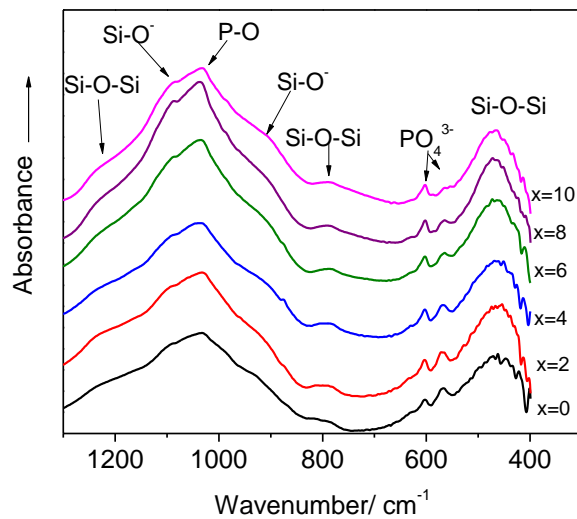


**Fig. 3**  FTIR spectra of the $56SiO_2 \cdot (40-x)CaO \cdot 4P_2O_5 \cdot xAg_2O$ samples.

In the 550-610 cm$^{-1}$ spectral region absorption signals associated with P-O vibrations can be observed. A strong IR signal located between 850 and 1250 cm$^{-1}$ dominate the spectra and is given by the convoluted bands of stretching vibrational modes of $SiO_4$ and $PO_4$ tetrahedra. The shoulder situated around 1233 cm$^{-1}$ can be ascribed to the longitudinal optical Si-O-Si stretching vibration [7]. The absorption band located at 1090 cm$^{-1}$ is attributed to the stretching mode of Si-O$^-$ bonds in the $Q^3$ tetrahedral units, while the shoulder centered on 930 cm$^{-1}$ is given by the vibration of two non-bridging oxygen atoms in the Si-O-Si environment ($Q^2$ units) [8, 10]. The silanol vibrations give rise to a signal at 960 cm$^{-1}$, which is convoluted with that given by the $Q^2$ unit vibrations [11, 12]. The IR band at about 1034 cm$^{-1}$ can be associated with the P-O stretching vibrational mode of $PO_4^{3-}$ tetrahedra. An intense absorption signal occurs at 470 cm$^{-1}$

and can be assigned to the rocking motion of the bridging oxygen atoms perpendicularly to the Si-O-Si plane [7]. The bending motion of oxygen atoms along the bisector of the Si-O-Si bridging group give rise to the band centered on 800 cm$^{-1}$ [7]. A doublet corresponding to P-O asymmetric bending vibrations in the PO$^4$ tetrahedra was observed at 567 and 601 cm$^{-1}$ [13].

### 2.2.4    Surface area and pore structure analyses

For a better understanding of silver distribution in the glass matrix, textural analyses were also performed. According to IUPAC classification the isotherms obtained from the samples are type IV and type II isotherms, implying that each of these samples contains mesopores, i.e. pores with diameters in the range 2–50 nm [14] (See Fig. 4), and exhibit type H1 hysteresis loops typical of large pore ordered mesoporous silica for the samples with 0≤x≤6 and type H3 hysteresis loops for the samples with x=8 and x=10, respectively (Fig. 5) [15].
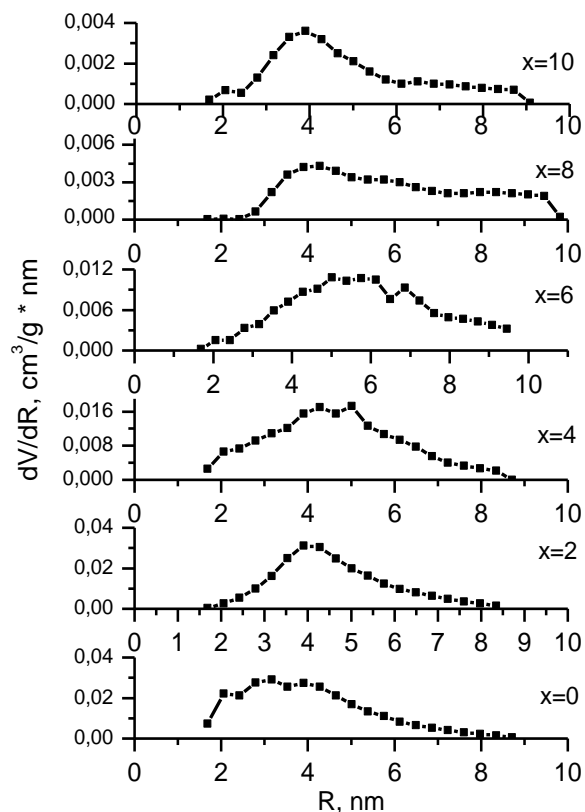


**Fig. 4.** Textural pore size distribution of the 56Si0$_2$·(40-x)CaO·4P$_2$O$_5$·xAg$_2$O samples.

This morphological behavior could be caused by the potential presence of Ag nanoparticles that are deposited on the pore walls and block the pores. Another reason enforcing this assumption that the pores are gradually being field with silver nanoparticles is the fact that the specific surface area of the samples decreases with the increasing of the silver concentration. The data are reported in Table 1

**Table 1**. Textural properties of the $56SiO_2 \cdot (40-x)CaO \cdot 4P_2O_5 \cdot xAg_2O$ samples.

| x (wt %) | Pore volume $(cm^3/g)$ | BJH maximum pore radius (nm) | BJH median pore radius (nm) | BET Surface area $(m^2/g)$ |
|---|---|---|---|---|
| 0 | 0.26 | 3.05 | 3.82 | 118.37 |
| 2 | 0.22 | 4.05 | 4.39 | 76.16 |
| 4 | 0.16 | 4.96 | 4.57 | 63.21 |
| 6 | 0.13 | 5.92 | 5.75 | 37.19 |
| 8 | 0.05 | 4.11 | 5.59 | 16.53 |
| 10 | 0.03 | 3.87 | 4.42 | 12.30 |

A progressive decrease of total pore volume occurs, the value is diminished more than eight times, from 0.26 to 0.03 $cm^3g^{-1}$ with increasing $Ag_2O$ content. These changes, which occur as a result of the increasing of $Ag_2O$ concentration, could be due to the progressive decreasing of the viscosity that is expected to occur as the silver content becomes higher. Fig. 4.7 shows nitrogen adsorption/desorption isotherms of the different silver containing samples sintered at 580ºC.

The textural properties expressed in terms of pore size distributions obtained from the desorption branch of the nitrogen sorption isotherms using BJH analysis are illustrated in Fig. 4 as a function of silver content. One can see a progressive broadening of the mesopores distribution as the silver content increases. This behavior becomes more visible for the sample with $x \geq 4$.

### 2.2.5 *UV-vis*

UV-vis absorption spectra (Fig. 5) were further recorded in order to get more information on the structure of the investigated samples. The electronic absorption band located between 220 and 300 nm is present in all investigated samples, but it is clearly evidenced in the glass matrix spectrum, where its maximum appears at 217 nm. Typically, the $Ag^+$ signature can be seen inside of the spectral region between 200 and 250 nm, and, therefore, the analysis of this signal becomes difficult.
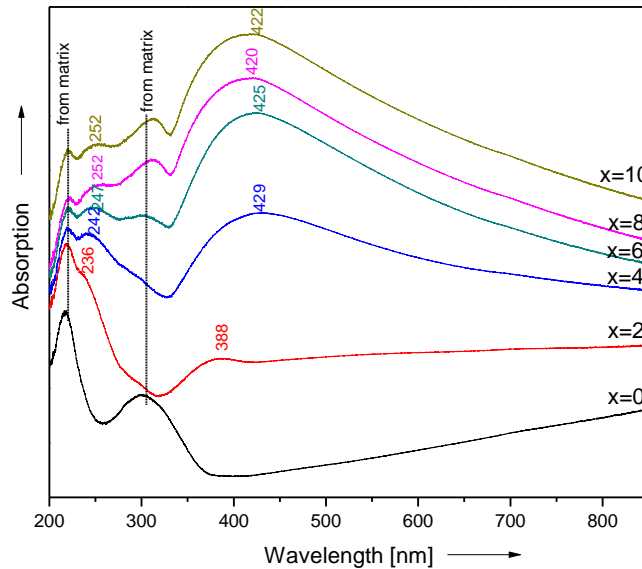


**Fig. 5** UV-vis absorption spectra of the $56SiO_2 \cdot (40-x)CaO \cdot 4P_2O_5 \cdot xAg_2O$ samples.

However, a shift of the maximum value of this band from 217 to 221 nm can be observed as silver amount increases. Moreover, an absorption signal around 240 nm increases in intensity as the silver content becomes higher than 4 mol%. These spectral behaviors could be associated with the raise of the number of silver ions and recommend the use of these samples as potential biomaterials with antimicrobial properties. The absorption around 420 nm in the UV-VIS spectra of the samples with x=4, 6, 8 and 10 is attributed to the presence of silver nanoparticles [18]. The asymmetry of this broad band comes from the convolution of the signal given by individual silver nanpoarticles with that associated with the existence of silver clusters that arises at higher wavelengths [19, 20].

It is justified to assume that the appearance of the absorption signal at around 390 nm in the spectrum of the sample with 2 mol% $Ag_2O$ (Fig. 5) is mainly due to the existence of almost spherical silver nanoparticles having small dimension within the glass matrix. What concerns the samples with higher silver content, the absorption maximum at 420-430 nm is caused by nonspherical silver particles or/and particles with higher sizes. The appearance of less spherical nanoparticles as silver particles become larger was also previously observed [23].

### 2.2.6 TEM

In order to validate the assumed hypothesis concerning the presence of Ag nanoparticles, TEM images were recorded and analyzed. The TEM pictures prove for all $Ag_2O$ containing samples that the silver is present as nanoparticles and/or nanosized silver clusters of various dimensions and shapes, inside the composites glass matrix, depending on the silver oxide content (Fig. 6)
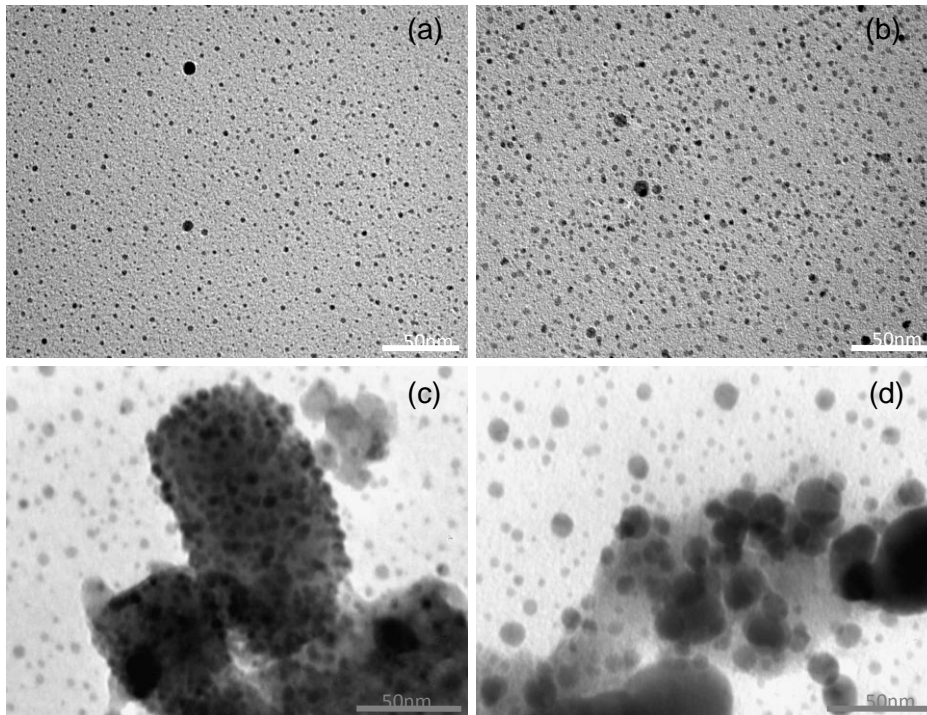


**Fig. 6** TEM images of the $56SiO_2 \cdot (40-x)CaO \cdot 4P_2O_5 \cdot xAg_2O$ samples
(a) x=2, (b) x=4, (c) x=8, (d) x=10
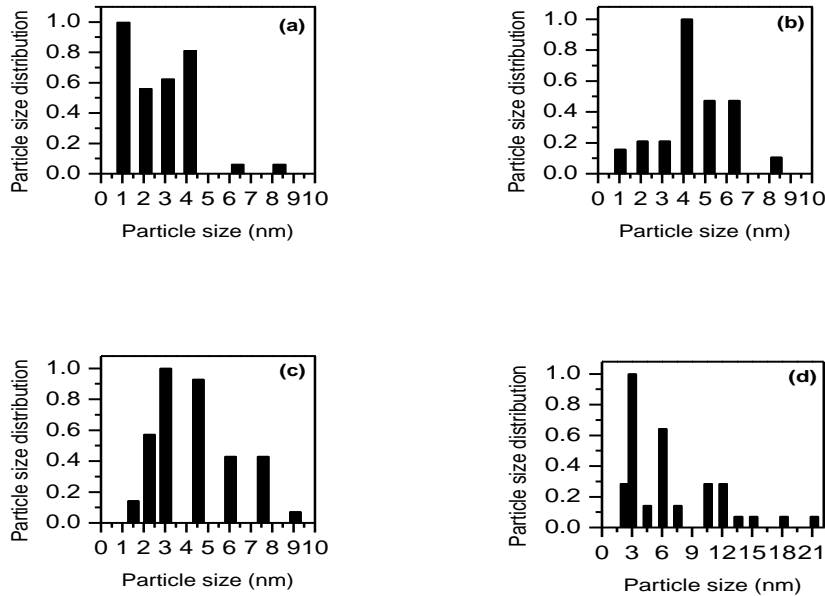
**Fig. 7** The normalized size distribution of the silver nanoparticles obtained from the TEM pictures analysis of the $56SiO_2 \cdot (40-x)CaO \cdot 4P_2O_5 \cdot xAg_2O$ samples (a) x=2, (b) x=4, (c) x=8, (d) x=10

For the sample containing 2 mol% $Ag_2O$ (Fig. 8a) one can observe a distribution of silver particles with almost spherical shapes and sizes in the range between 1.5 and 4 nm (Fig7a). By looking at the particles size distributions derived from the TEM images of the silver/bioactive glass composites with 4, 8 and 10 mol% $Ag_2O$, which are presented in Figs. 7b, 7c and 7d, one can remark the spreading of a relatively high number of silver particles with different sizes that occurs as the $Ag_2O$ content increases. For the samples with the higher silver content (x=8 and x=10) one can see spherical and nonspherical particles with dimensions of tens nanometers.

## 2.3  Bioactivity studies

The bioactivity was investigated by soaking the materials in SBF at 37 ºC to study de hydroxyapatite/carbonated hydroxyapatite (HA/HCA) formation by XRD, FTIR, SEM observation, EDS analysis, and XPS. It were selected 3 samples with x=0, x=2 and x=8 silver content. In vitro tests were carried out by soaking the samples in SBF according with Kokubo composition up to 14 days.

## 2.3.1 XRD

XRD analyses performed after SBF immersion allow to verify how silver content influences the self-assembling process on samples surface induced by the ionic exchange between the glasses and the SBF solution.
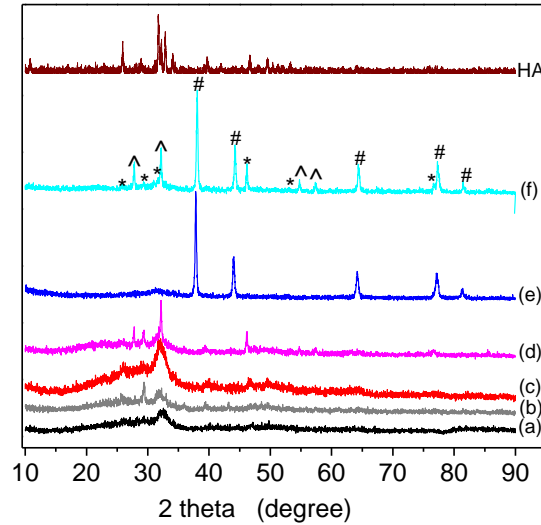


**Fig. 8** XRD pattern of the $56SiO_2 \cdot (40-x)CaO \cdot 4P_2O_5 \cdot xAg_2O$ samples: (a) x=0, (c) x=2 and (e) x=8 prior to SBF soaking; (b) x=0,(d) x=2 and (f) x=8 after SBF soaking (**\*** -HA, **#** -Ag, ^ -$Ag_3PO_4$)

The XRD patterns of non immersed samples already shows a broad halo of the non-crystalline calcium phosphosilicate matrix (x=0), with a maximum centered at $2\theta=32°$ and weak features of an apatite like phase with nanosized crystallites. In order to clearly distinguish the apatite phase a standard hydroxyapatite (HA) pattern [25] was inserted in Fig. 8. For the sample without silver only the strongest lines relative to HA is evident, while after soaking in SBF (14 days) new peaks corresponding to crystallized HA phase appear. For the sample with x=2 one can observe small peaks that can be attributed to metallic silver, but also to silver oxide crystals. After SBF immersion these signals grow in intensity, and some new peaks attributed to $Ag_3PO_4$ phase appear [26]. The sample with high silver concentration exhibits the same behavior as the one with x=2, but in this case the new crystalline phases formation is more evident.

## 2.3.2   FTIR

The FTIR spectra of silver free and silver containing samples before and after soaking in SBF for *in vitro* bioactivity tests are illustrated in Fig.9 together with the spectrum of pure HA [25]. The presence of the bands at 569, 605, 1040 cm$^{-1}$ are attributed to the [$PO_4$] unit vibrations corresponding to the crystalline HA. These bands are clearly visible also for the non immersed samples. Besides these peaks one can observe in the spectra of non immersed samples the presence of the band at 1080 cm$^{-1}$ attributed to the stretching vibration of Si-O bonds and of the shoulder around 950 cm$^{-1}$, due to the vibration of Si-O-Si groups. The strong band around 470 cm$^{-1}$ is attributed to the *Si–O–Si* bond bending motion. The FT-IR spectra of the samples incubated in SBF solution show, in addition to phosphate bands, a new band at 870 cm$^{-1}$ assigned to carbonate ions that indicate the formation of a carbonate apatite phase. By analyzing the IR signal given by the sample with x=8, after SBF incubation, a decrease in the intensity of the bands situated at 569, 605 cm$^{-1}$ and associated with the presence of [$PO_4$] unit vibrations can be observed. The  incorporation of carbonate ions in the HA layer may occur by ion exchange mechanism, where $CO_3^{2-}$ ions from the SBF partially replace the $PO_4^{3-}$ ions, and these phosphate ions react with silver and form $Ag_3PO_4$ crystals that are visible in SEM images.
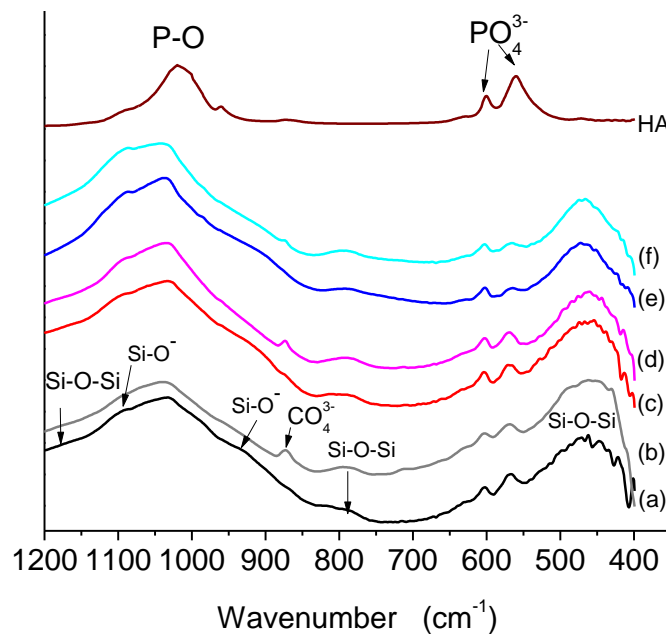


**Fig. 9** FTIR spectra of the $56SiO_2 \cdot (40-x)CaO \cdot 4P_2O_5 \cdot xAg_2O$ samples: (a) x=0,(c) x=2 and (e) x=8 prior to SBF soaking; (b) x=0,(d) x=2 and (f) x=8 after SBF soaking.

### 2.3.3 SEM/EDS

Fig. 10 shows the SEM images of the three samples before and after soaking in SBF. The HA/HCA layer is clearly visible on the surface of the SBF immersed samples (Fig. 10b, e, h), and the HA crystals size increases with the increasing of silver concentration (Fig. 10h). By analyzing the SEM images, performed with back scattered electrons, well defined $Ag_3PO_4$ sub-microcrystals were observed in the silver containing sample [27].
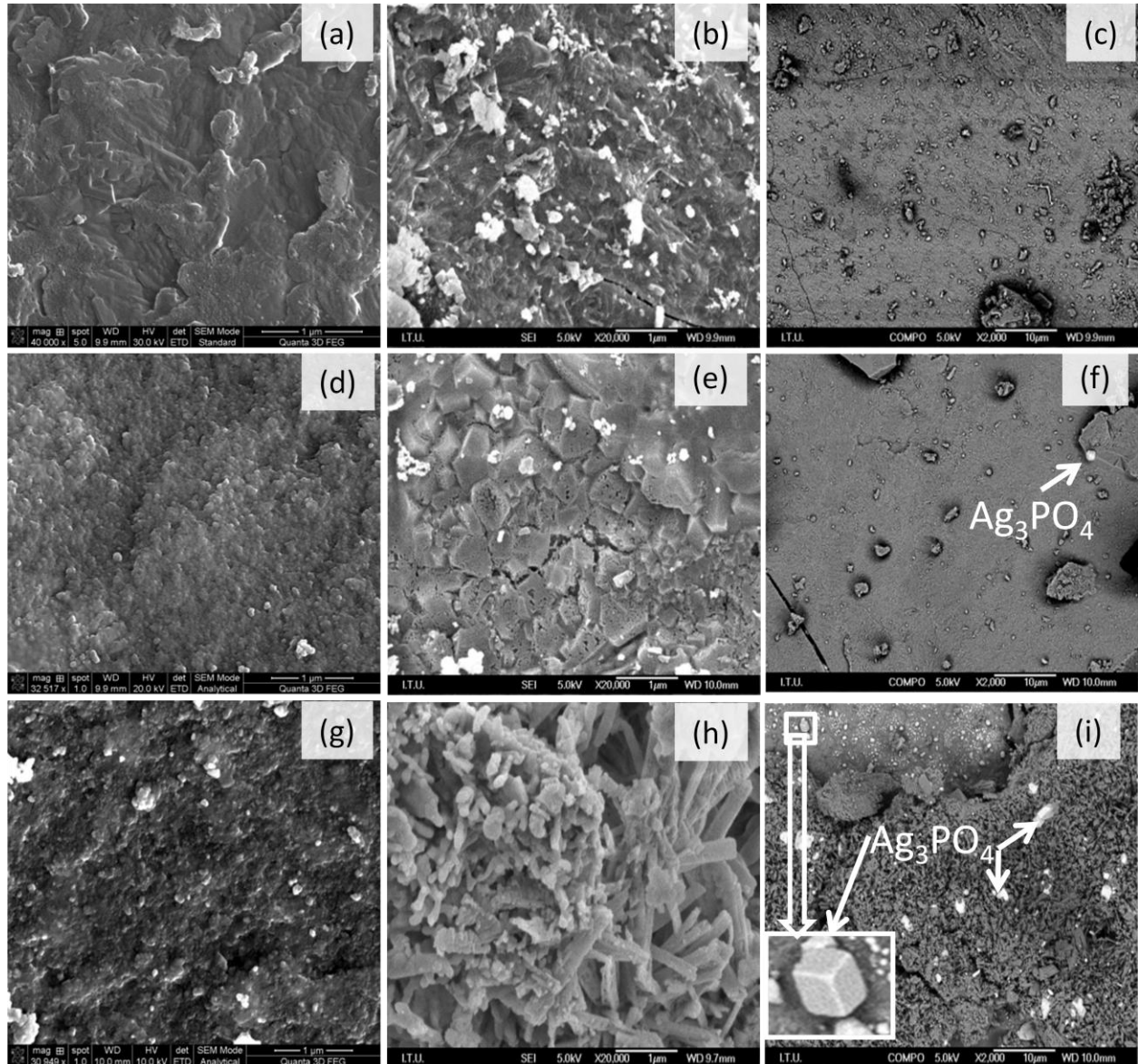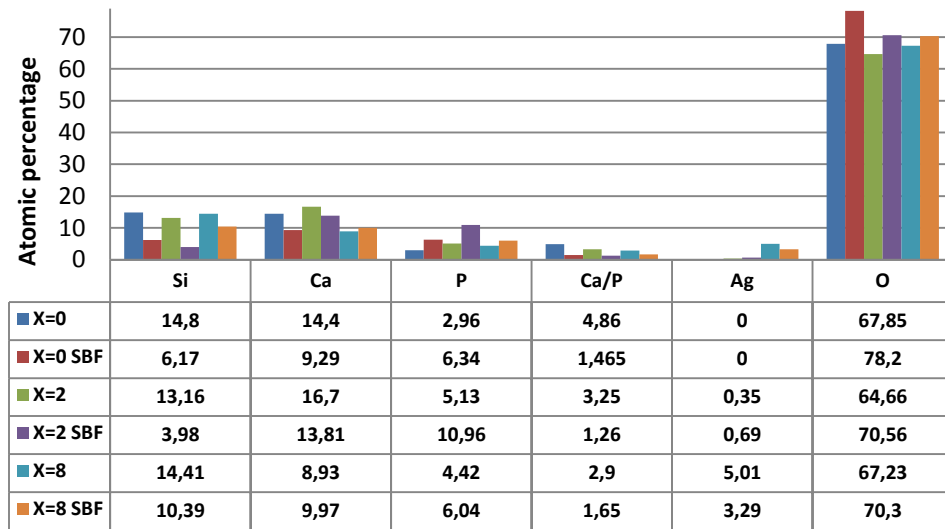


**Fig. 10** SEM images of the bioactive glass samples with different silver content: (a) x=0, (d) x=2 and (g) x=8 prior to SBF soaking; (b) x=0,(e) x=2 and (h) x=8 after SBF soaking; (c) x=0,(f) x=2 and (i) x=8 back scattered electron images after SBF soaking

This crystalline phase was also observed in the XRD pattern of SBF soaked silver containing samples.-For a better understanding of the SEM images EDS analyses were also conducted, the result being presented in Table 2 It can be seen that the Ca:P ratio decreases after the SBF soaking and for the compound with 8% silver this ratio (1.65) is very close to the theoretical value of pure HA (1.67).

**Table 2** Elemental composition in at % obtained from EDS analysis of the $56SiO_2 \cdot (40-x)CaO \cdot 4P_2O_5 \cdot xAg_2O$ samples prior and after SBF soaking

| | Si | Ca | P | Ca/P | Ag | O |
|---|---|---|---|---|---|---|
| X=0 | 14,8 | 14,4 | 2,96 | 4,86 | 0 | 67,85 |
| X=0 SBF | 6,17 | 9,29 | 6,34 | 1,465 | 0 | 78,2 |
| X=2 | 13,16 | 16,7 | 5,13 | 3,25 | 0,35 | 64,66 |
| X=2 SBF | 3,98 | 13,81 | 10,96 | 1,26 | 0,69 | 70,56 |
| X=8 | 14,41 | 8,93 | 4,42 | 2,9 | 5,01 | 67,23 |
| X=8 SBF | 10,39 | 9,97 | 6,04 | 1,65 | 3,29 | 70,3 |

### 2.3.4   XPS

The XPS survey spectra recorded for bioactive glasses with different silver content before and after immersion in SBF are presented in Fig. 11. The elemental composition recorded at the surface of the samples before and after immersion in SBF was also determined from XPS survey spectra and presented in Table 3. One should stress that the uncertainty of the measurements was of ±0.05.  From the data obtained for the samples incubated in SBF, one can see that the highest Ca:P ratio (4.46) was determined for the compound with 2 % Ag and lowest one (2.33) for the 8% silver containing bioactive glass. A special remark should be highlighted, namely, a high silver amount preferentially determines the formation of HA. The results also show a considerably increase of the relative atomic percent of carbon for the samples with silver, which represents another proof that the silver content favors the formation of carbonated apatite.
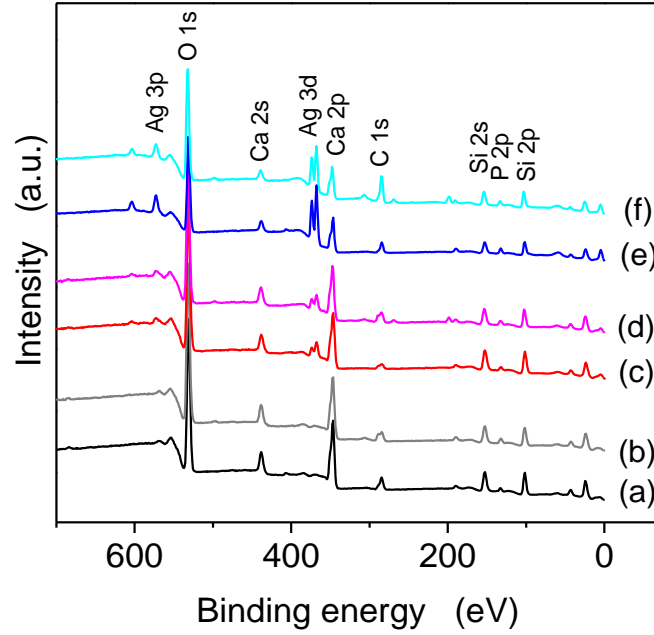
**Fig. 11** XPS survey spectra of the $56SiO_2 \cdot (40-x)CaO \cdot 4P_2O_5 \cdot xAg_2O$ samples: (a) x=0,(c) x=2 and (e) x=8 prior SBF soaking; (b) x=0,(d) x=2 and (f) x=8 after SBF soaking

**Table 3** Elemental composition in at % obtained from XPS measurements of the $56SiO_2 \cdot (40-x)CaO \cdot 4P_2O_5 \cdot xAg_2O$ samples prior and after SBF soaking



|          | Si    | Ca    | P     | Ca:P | Ag   | O     | C     | Cl   |
|----------|-------|-------|-------|------|------|-------|-------|------|
| x=0      | 21,79 | 13,46 | 1,93  | 6,97 | 0    | 49,93 | 12,86 | 0    |
| x=0 SBF  | 18,74 | 12,87 | 3,008 | 4,27 | 0    | 52,57 | 12,8  | 0    |
| x=2      | 25,22 | 12,15 | 2,27  | 5,35 | 1,11 | 52,16 | 7,06  | 0    |
| x=2 SBF  | 18,37 | 11,83 | 2,65  | 4,46 | 1,17 | 49,65 | 14,73 | 1,57 |
| x=8      | 21,67 | 9,74  | 4,21  | 2,31 | 5,78 | 44,29 | 14,29 | 0    |
| x=8 SBF  | 17,83 | 7,23  | 3,09  | 2,33 | 3,41 | 38,91 | 26,75 | 2,74 |

Furthermore, the XPS Ag 3d high resolution spectra appear broader and asymmetric evidencing a shoulder at lower binding energy that signalizes the presence of new type of bonds.

The deconvolution of Ag 3d photoelectron peaks (Fig. 12) shows for Ag $3d_{5/2}$ line two components at the binding energies around 368.5 eV and 367 eV corresponding to metallic silver and silver oxide, respectively (Fig. 12) [28]. After immersion in SBF solution, the Ag $3d_{5/2}$ line is well fitted with four components. The new components occur at 367.9 eV and 364.7 eV. The component recorded around 367.9 eV is attributed to $Ag_3PO_4$ [29]. One should emphasize that the signature of this structure was also evidenced in XRD patterns and SEM images. The component at lower binding energy, about 365 eV, may be associated to AgCl formation that seems very likely, as a visible amount of chlorine was evidenced after immersion in SBF solution (Table 3).
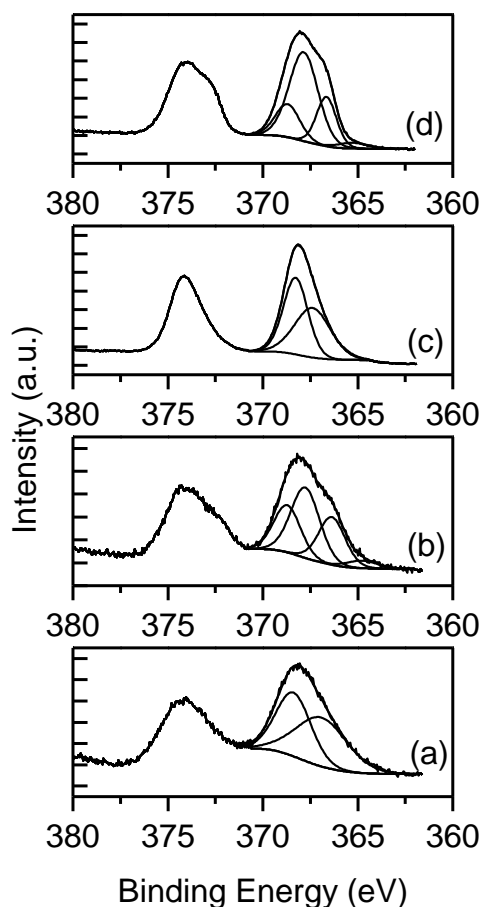


**Fig. 12** Deconvoluted XPS Ag 3d high resolution spectra of the $56SiO_2 \cdot (40-x)CaO \cdot 4P_2O_5 \cdot xAg_2O$ samples prior and after SBF soaking: (a) x=2 prior SBF, (b) x=2 after SBF(c) x=8 prior SBF and (d) x=8 after SBF soaking

### 2.3.5 Antibacterial studies

Antibacterial tests were caried out by difusion method on powder samples using a dilution of 1% on staphylococus aureus and on escherichia coli. The antibacterial activity was evaluated by measuring the zone of inhibition against the test organism. The results are presented in Fig. 13. The sample with the highest silver content (x=10) produced the higest zone of inhibition against both S.aureus and and E.coli. However the gram-negative bacteria (E. coli) was less sensitive than the gram-positive one (S. aureus) on all silver containing samples. For the silver free sample it cannot be observed any antibacterial effect.



|          | x=0 | x=2 | x=4 | x=6 | x=8 | x=10 |
|----------|-----|-----|-----|-----|-----|------|
| ■ S. aureus | 0 | 9 | 7 | 11 | 13 | 13 |
| ■ E.Coli | 0 | 6 | 6 | 10 | 11 | 12 |
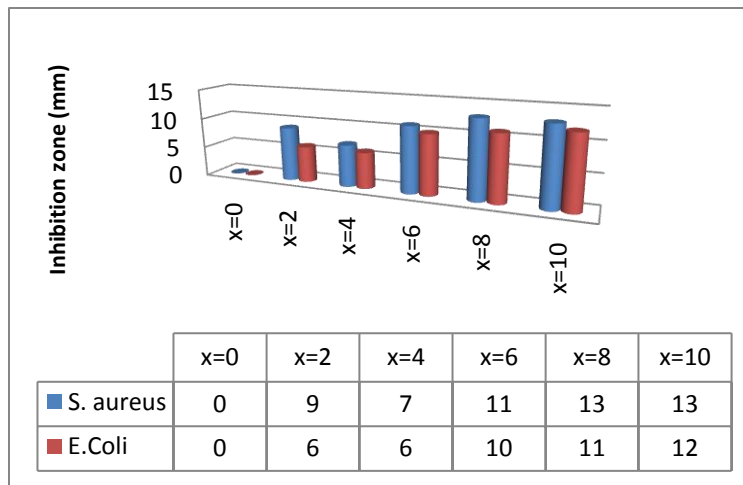
**Fig. 13** Inhibitory zone test results of the $56SiO_2 \cdot (40-x)CaO \cdot 4P_2O_5 \cdot xAg_2O$ samples

### 2.3.6 Protein adsorption studies

Protein binding capability to the bioactive glasses surface was investigated by cw-EPR experiments and XPS measurements. For this reason there were selected 3 samples: the silver free one (x=0), one with low silver concentration (x=2) and a high silver concentration (x=8). In order to investigate the protein-binding capability of the bioglass, the surfaces were functionalized with horse methemoglobin. This protein has a molecular mass of 66.5 kDa and a diameter of about 5.6 nm (1ZLU, Protein Data Bank). Hemoglobin molecule is an assembly of four polypeptide chains (two β-chains and two α-chains), and each protein chain contains a heme group whose iron ion binds reversibly with one oxygen molecule. In methemoglobin the iron is oxidized to $Fe^{3+}$, inhibiting the oxygen-binding capabilities of the protein.

Horse methemoglobin has 2 native cysteines accessible for spin labels, situated in position β-93 from the two β chains. These cysteines were labeled with (1-oxyl-2,2,5,5-tetramethylpyrroline-3-methyl) methanethiosulfonate spin label (MTSSL) (see Fig. 14).
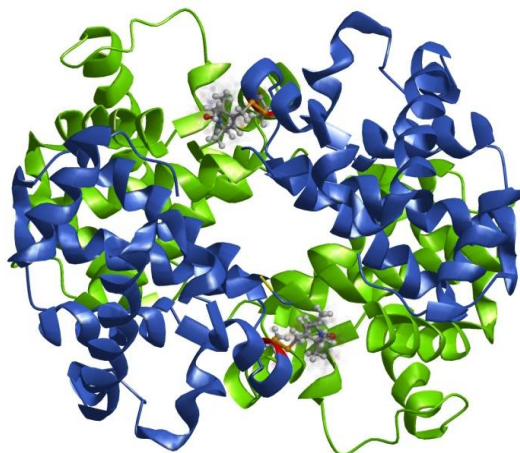


**Fig. 14** Structure of methemoglobin obtained by X-ray crystallography (1ZLU from Protein Data Bank). The α-chains are colored in green and the β-chains are colored in blue. The native cysteines from position β-93 are colored in red and for each position β-93 all possible rotamers for MTSSL are shown (populations calculated for room temperature (298 K));

For this measurements powder samples were incubated for 4 hours at 37°C in a solution of 22.5 mg/ml (300 μM) horse methemoglobin in phosphate buffer (0.01M, pH 7.4) with low salt concentration (10 mM NaCl). After immersion the samples were washed three times with buffer solution, to remove the detachable protein molecules from the surface. Prior functionalization, horse methemoglobin was spin-labeled with MTS in position β-93.

### 2.3.6.1 RES

X-band cw-EPR spectra recorded at room temperature for methemoglobin in solution and after adsorption onto bioactive glasses with different silver content are shown in Fig. 15. In all EPR spectra were identified two components, which correspond to spin label populations with different mobility.
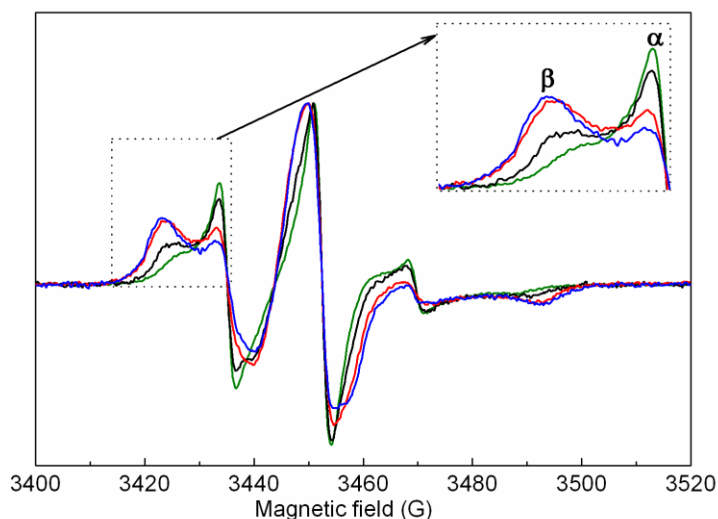
**Fig. 15** Room temperature X-band cw-EPR spectra of horse methemoglobin spin-labeled in position β-93* recorded in solution (green), and in in adsorbed state, immediately after immersion on bioactive glass with 0 % (black), 2 % (red), and 8 % (blue) of silver content respectively. The mobile and immobile components visible in the lower field spectral lines are depicted with α and β respectively (inset)

In solution, the mobile EPR component (α in Fig. 4.20) arises from the surface exposed spin labels (which point out of the protein, such that some flexibility is allowed), while the immobilized component (β in Fig. 4.20) is interpreted as corresponding to the spin labels trapped in a protein pocket (the so called tyrosine pocket, due to the penultimate residue being Tyr β145).

This interpretation is in agreement with the results obtained by Moffat [30] for horse methemoglobin spin labeled with 4-(2-Iodoacetamido)-2,2,6,6-tetramethyl-1-piperidinyloxy) in position β-93.

Upon adsorption of protein on bioactive glass the equilibrium between the two conformations is significantly shifted towards the component β (see Fig. 4.20). The spin labels of this fraction interact with the surface of the bioactive glass or with adjacent folded parts of protein and the observed shift of the equilibrium between immobile and mobile states suggests that the environment of the β-93* residue is perturbed by the adsorption process. The increasing of silver content in the bioactive glass leads to further immobilization of the protein. Methemoglobin becomes more rigid as a consequence of interaction between spin label and silver ions that are disposed at the surface of the bioactive glass. The explanation can be based on

the fact that $Ag^+$ reacts with thiol groups in proteins, due to the high affinity between the soft sulfide and the soft metal [31, 32] . Although the protein was labeled with MTS spin label and, therefore, the cysteine sulfur is blocked by the spin label and thus not accessible for Ag, the labeling efficiency was 50%, so there are unlabeled cysteines in the sample. We assume that these cysteines, which do not carry a spin label interact with Ag, and consequently, unlabeled molecules bind easier than spin labeled protein. This interaction can induce a closer packing of methemoglobin on the surface, which would lead to enhanced interaction of the spin label side chain with neighboring protein atoms. Protein-binding capability of the Ag containing bioactive glasses was also investigated by means of XPS analysis, method that supports the conclusions from EPR measurements

### 2.3.6.2  XPS

Protein-binding capability of the silver containing bioactive glasses was also investigated by means of XPS analysis (Fig. 16). The effect of silver content on adsorption of methemoglobin from solution is reflected by the evolution of the new N 1s and S 2p photoelectron peaks, and by the great amount of C 1s recorded after immersion in protein solution.
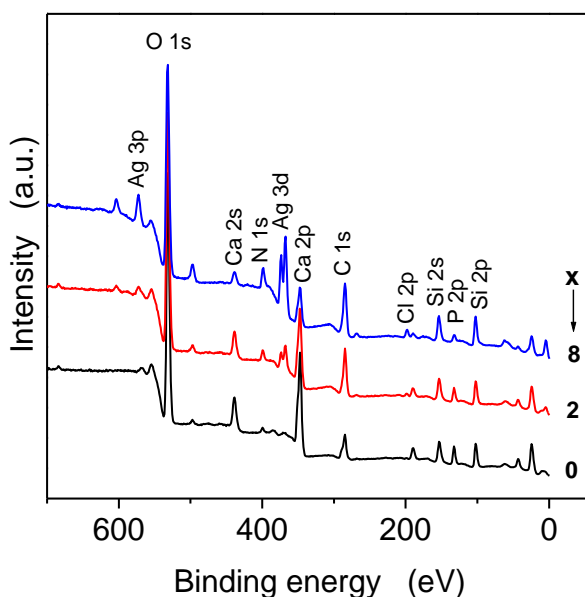


**Fig. 16** XPS survey spectra of the $56SiO_2 \cdot (40-x)CaO \cdot 4P_2O_5 \cdot xAg_2O$ samples after protein attachment

The amounts of each of these elements were found to increase significantly with the silver content (Table 4), while the amounts of the main elements were reduced due to the protein coverage of the surface. The nitrogen concentration was practically zero before immersion and considerably increased after immersion due to protein attachment [33, 34].

**Table 4** Elemental composition in at % obtained from XPS analysis of 56SiO2·(40-x)CaO·4P2O5·xAg2O glass samples prior to and after protein binding.



| | Si | Ca | P | Ag | O | C | N | S | Fe |
|---|---|---|---|---|---|---|---|---|---|
| x=0 | 21,79 | 13,46 | 1,93 | 0,00 | 49,93 | 12,86 | 0,00 | 0,00 | 0,00 |
| x=0 Hgb | 13,47 | 12,65 | 6,65 | 0,00 | 49,32 | 15,99 | 1,19 | 0,70 | 0,00 |
| x=2 | 25,22 | 12,15 | 2,27 | 1,11 | 52,16 | 7,06 | 0,00 | 0,00 | 0,00 |
| x=2 Hgb | 12,31 | 8,99 | 4,81 | 1,11 | 43,42 | 25,95 | 2,59 | 2,59 | 0,00 |
| x=8 | 21,67 | 9,74 | 4,21 | 5,78 | 44,29 | 14,29 | 0,00 | 0,00 | 0,00 |
| x=8 Hgb | 15,49 | 4,34 | 2,29 | 3,08 | 37,84 | 27,93 | 4,96 | 1,41 | 2,62 |
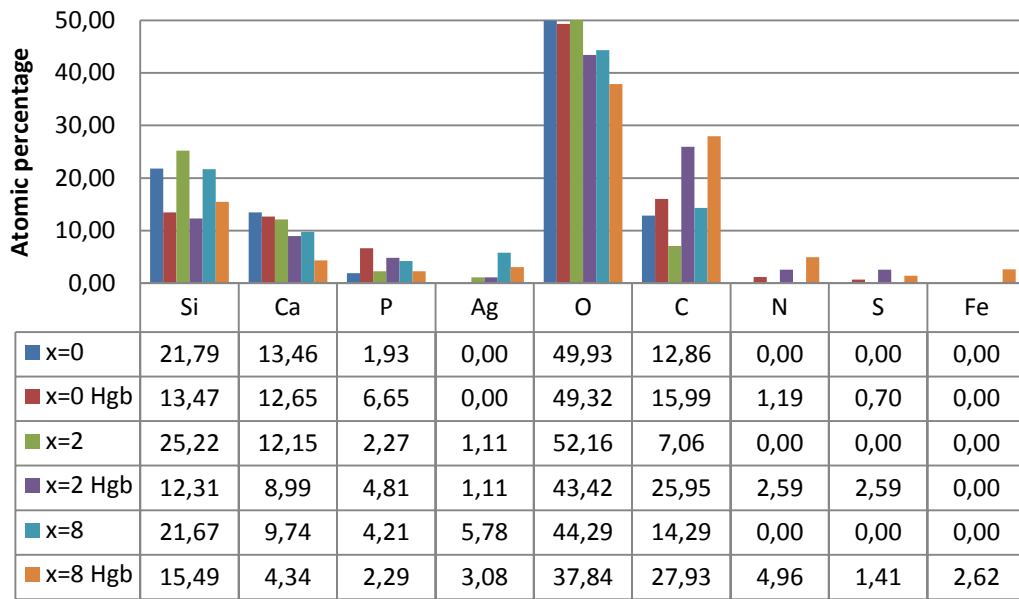
This result clearly shows a larger coverage with protein for the sample with higher silver content. On the other hand, not only the amount of the adsorbed protein but also the protein conformation is important for further cell proliferation on these materials [35]. In this respect, both EPR and XPS measurements reported the highest agglomeration of protein molecules on bioactive glass with 8 % silver content, pointing out that in this case the protein is somehow "forced" by the neighbor molecules to keep its compact structure. Accordingly, increasing of silver concentration up to 8% might prevent protein unfolding on bioactive glass surface.
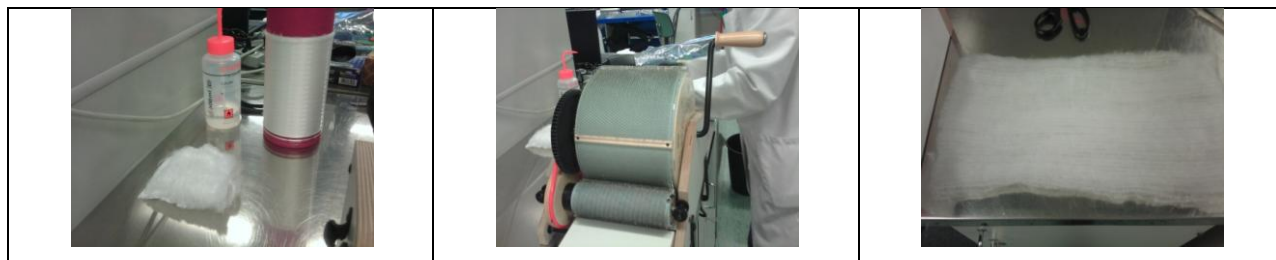
# 3 POLYMER\SILVER-BIOACTIVE GLASS COMPOSITES

The composites consist of poly-D,L-lactic acid nonwoven textiles coated with sol-gel derived bioactive glasses. The polymer textiles were made from a commercially available Poly-96L/4D-lactide copolymer fiber containing 16 filaments provided by Tampere University of technology from Tampere, Finland and the bioglasses were prepared by sol-gel-derived glass containing Ag nanoparticles in the system $56SiO_2$-$36CaO$-$4P_2O_5$-$4Ag_2O$ (mol %) and its three-component counterpart $56SiO_2$-$40CaO$-$4P_2O_5$.

### 3.1.1 Polymer textile fabrication

For the fabrication of textiles there were used 4 km of Poly-96L/4D-lactide copolymer fibers provided by Tampere University of Technology from Tampere, Finland. The fibers were uniformly combed to a roll little by little and a fabric with a parallel orientation of fibers was obtained. The fabric was cut in 4 pieces. Every two pieces were overlaid taking care to obtain perpendicular orientation of the fibers from the two fabric sheets, and there were processed in a needle pouncing machine that contained a matrix of needles that went through the fabric several times giving it a pattern.



**Fig. 17.** Fabrication of Poly-96L/4D-lactide copolymer fabric: (A) Poly-96L/4D-lactide copolymer fibers, (B) Fiber roller comb, (C) obtained polymer fabric

### 3.1.2 Obtaining of bioactive glass/polymer composites

The obtained polymer meshes were coated with bioactive glass particles using aqueous slurry dipping as the processing method. Because of the poor adherence of the bioactive glass coating to the polymer fabric, another component in the coating slurry was added, that acted as glue promoting the adhesion of the glass particles to mesh surfaces. This component was polyvinyl alcohol (PVA) which is also a polymer. After several tests, a final slurry composition of 60% w/v of bioactive glass in 4% PVA solution was obtained. Pieces of 10x10 mm of fabric

were first pre treated in ethanol for 30 minutes to improve wetability, washed with distillate water and lowered in the slurry using tweezers and left immersed for 3 min under continuous slow steering to avoid precipitation of bioactive glass powder. After withdrawing, the samples were set on a glass to dry at room temperature. During the first half hour they were turned very often, once every two minutes. The obtained composites were left to dry for 3 days at room temperature for 3 days.

### 3.1.3  Characterization

The microstructure of the composites was studied by SEM and EDS analyses. Differential thermal analysis (DTA) and thermogravimetric analysis (TG) were used to verify the thermal degradation temperatures of these composite materials and to quantify the bioactive glass content on the polymer meshes.

### 3.1.3.1  SEM

The surface morphology of the polymer and the composites are presented in Fig. 18. As one can see the PLA sample presents voids between the fibers, showing an overall porous structure. The PLA+PVA hybrid composite polymer sample presents a thin film between the PLA fibers associated with PVA. Bioactive glass particles are angular in shape and are caught between the PLA polymer fibers with PVA.
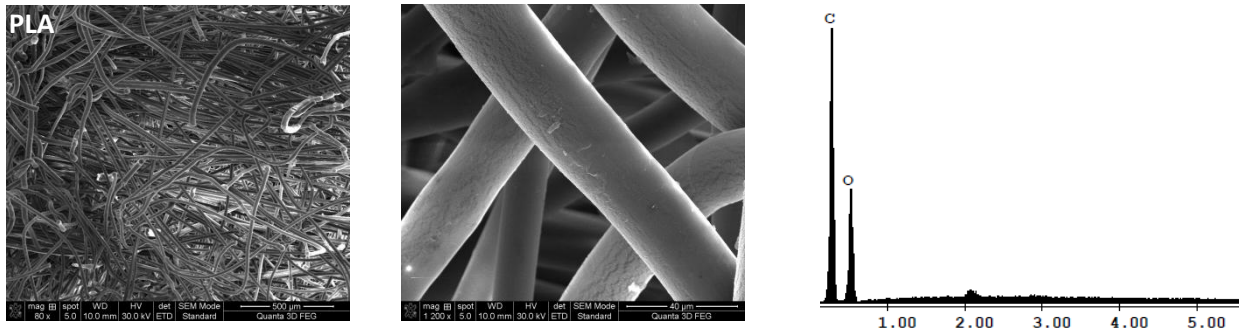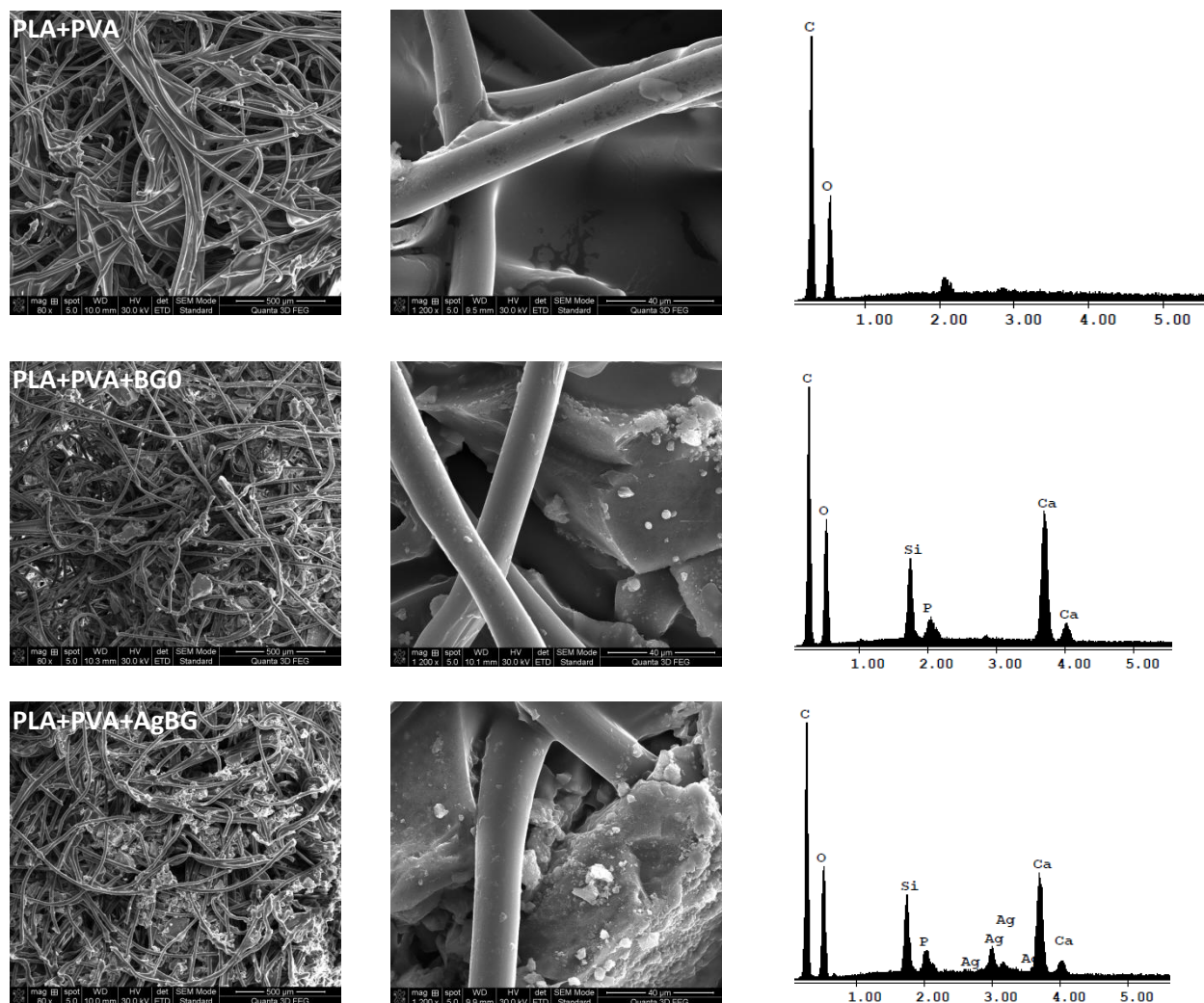
**Fig. 18.** SEM images of the polymer respectively polymer/ bioactive glass samples at low and high magnification and their corresponding EDS spectra

### 3.1.3.2   DTA/TG

Differential thermal analysis (DTA) and thermogravimetric analysis (TG) were used to verify the thermal degradation temperatures of these composite materials and to quantify the bioactive glass content on the polymer meshes [37]. The weight percentage of bioactive glasses was estimated from the difference in percentage mass, of the composites, at the beginning and at the end of each DTA run, where the polymer was assumed to be totally thermally degraded. In order to support this assumption DTA/TG analysis were performed also on the two types of polymers used for the preparation of the composites both individually and together.

By inspecting the DTA (Fig. 19 B) curve of PLA fiber meshes one can observe the glass transition temperature $T_g$ around 73 ºC, which is followed by melting behavior around 159 ºC. $T_g$ and the melting temperature $T_m$ strongly depend on molecular weight. Both $T_g$ and $T_m$ increase with molecular weight and reach constant values beyond molecular weight 20.000. It is important to note that $T_g$ is influenced by the degree of crystallinity in PLA [38]. The decomposition of PLA starts around 260 ºC. The decomposition is rapid at this temperature and it completes at 380 ºC. The DTA curve of PLA presentedin Fig. 4.25B that shows two not well separated endothermic peaks at around 364 ºC and 384º, respectively, with a corresponding massive weight loss,  as shown in the TG curve,  that is associated with the complete dissolution of PLA. A total of 97% of weight loss was observed in the decomposition of PLA [39].

By looking at the TG (Fig. 19A) curve corresponding to neat PVA polymer one can observe two distinct and well separated weight-loss turns with two corresponding weight loss peaks in the DTA curve. The first stage of decomposition (250– 350°C) corresponds mainly to elimination reaction of hydroxyl side groups, while the second degradation stage (above 380°C) is dominated by chain-scission and cyclization [40, 41]. The first degradation stage is associated with a weight loss of 60%, and the second stage with 32% of weight loss. The events corresponding to glass transition and melting point could not be observed in case of this polymer. The initial molecular weight and the hydrolysis degree influenced the thermo-oxidative degradation of PVA under dynamic thermogravimetric conditions. Higher molecular weight caused greater complexity in the degradation process, whereas higher hydrolysis degree reduced the decomposition temperature of PVA [42-44].

For PLA+PVA sample can be observed a degradation pattern consisting of two stages like in the case of neat PVA sample, and it can be observed also the lower temperature events which appear in case of neat PLA   ($T_g$ point at around 73 ºC and melting point around 159 ºC). Among this samples the initial degradation temperature of PVA is the lowest, whereas that of PLA is the highest, and the one for PLA+PVA is somewhere between that is in agreement with the literature [41].
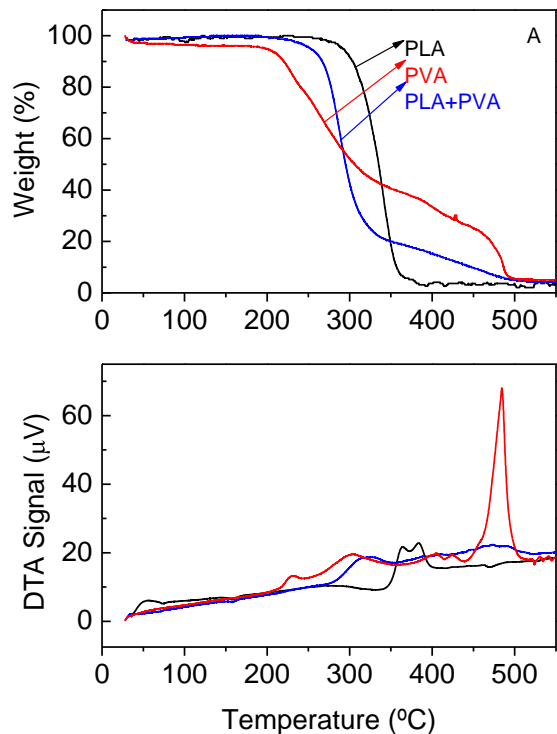
**Fig. 19** (A) and DTA (B) curves of polymers: PLA (black), PVA (red) and PLA+PVA (blue)
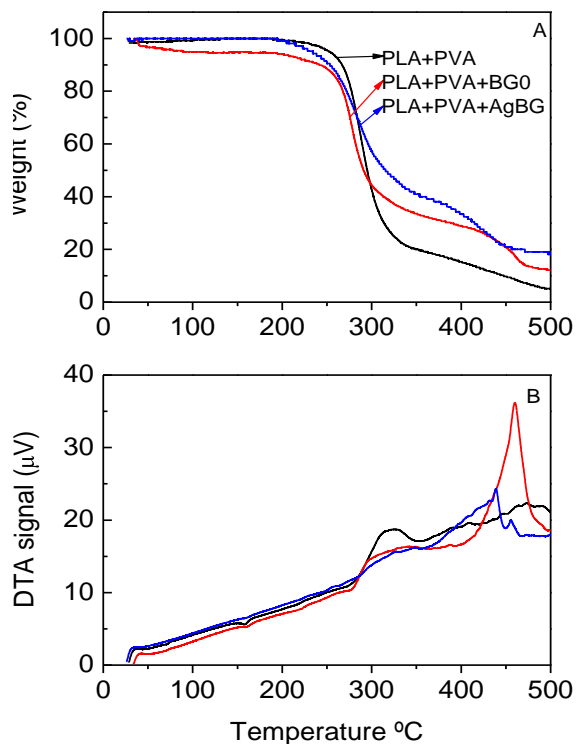
**Fig. 20** TGA (A) and DTA (B) curves of the composites PLA+PVA (black), PLA+ PVA+BG0 (red) and PLA+PVA+AgBG (blue)

The DTA signal given by the bioactive glasses containing composites exhibits the same behavior as the PLA+PVA polymer composite sample but the corresponding events happen at lower temperature as seen in Fig. 20. The shifts can be attributed to the better thermal conductivity of the bioactive glasses respectively of the silver. The weight percentage of bioactive glasses content in the composites was found to be 6.5% BG0 and 14.7% AgBG, respectively, suggesting more adhesion of the silver containing glasses to the polymer structure, thus confirming the SEM observations.
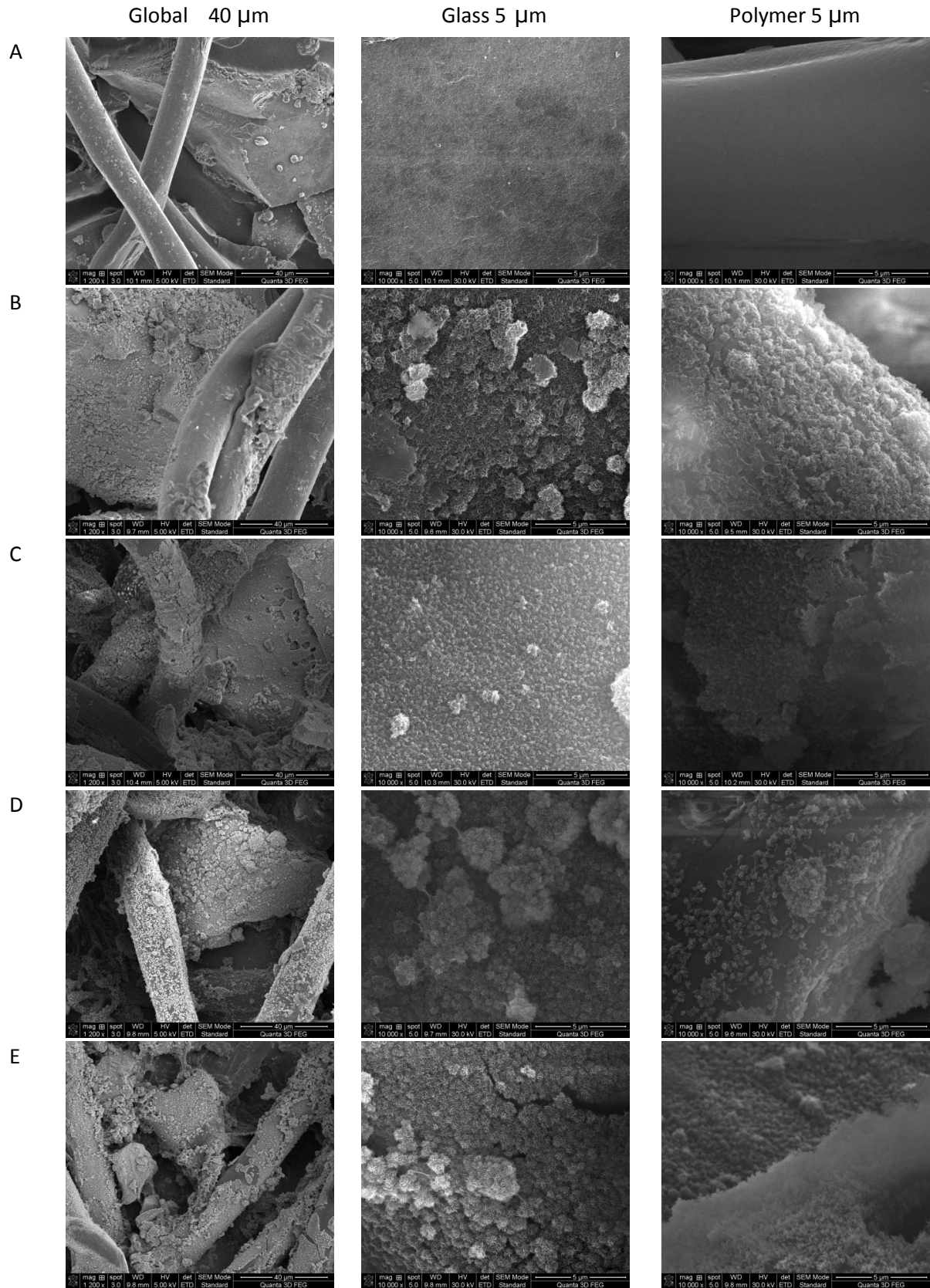
### 3.1.4   *Bioactivity*

This part of the study was carried out with the use of the standard acellular *in vitro* procedure described by Kokubo and colleagues. Pieces of 5x5mm of coated polymer fabrics were immersed in 25 ml of SBF in clean conical flasks, which had previously been washed using

HCl and deionized water. The conical flasks were placed inside an orbital shaker, which rotates at 100 rpm at controlled temperature of 37°C. The samples were extracted from the SBF solution after given times of 1, 7, 14, and 21 days. The SBF was replaced twice a week because the cation concentration decreases during the course of the experiments, as a result of the changes in the chemistry of the samples. Once removed from the incubation flasks, the samples were rinsed gently first in pure ethanol and then with deionized water and left to dry at ambient temperature.

The formation of HA on the surface of composites after immersion in SBF was investigated with analytical tools, such as SEM, XRD, XPS and IR spectroscopy, in order to assess the chemical reactivity of the materials.

### 3.1.4.1   SEM

Fig. 21 and Fig. 22 show SEM images of polymer meshes coated with BG0 and AgBG respectively after immersion for up to 21 days in SBF. First HA crystals developed in just 1 day of dynamic immersion in SBF. In addition to HA specific crystals, on the composite containing AgBG one can observe also silver phosphate crystals, which also develop from the first day immersion and do not inhibit HA crystal formation. This crystalline phase was also observed on the X-ray difractograms. As expected, the amount of HA crystals increased with the immersion time. This is visible also on the SEM images of the sample immersed in SBF for 21 days  [50]. The high magnification SEM images prove that HA is formed also on the polymer fibers not only on the bioactive glass phase from the composite. This results are also confirmed by EDX measurements presented in Table 5, were also can be seen that is no HA formation in the case of neat polymer samples.

|                  | Global    40 μm | Glass  5 μm | Polymer 5 μm |
|------------------|-----------------|-------------|--------------|
| A                |                 |             |              |
| B                |                 |             |              |
| C                |                 |             |              |
| D                |                 |             |              |
| E                |                 |             |              |

**Fig. 22** SEM images of Polymer/BG0 after incubation in SBF for: A-0, B-1, C-7, D-14, E-21, days

Global  40 µm                    Glass 5 µm                    Polymer 5 µm

A

B

C

D

E
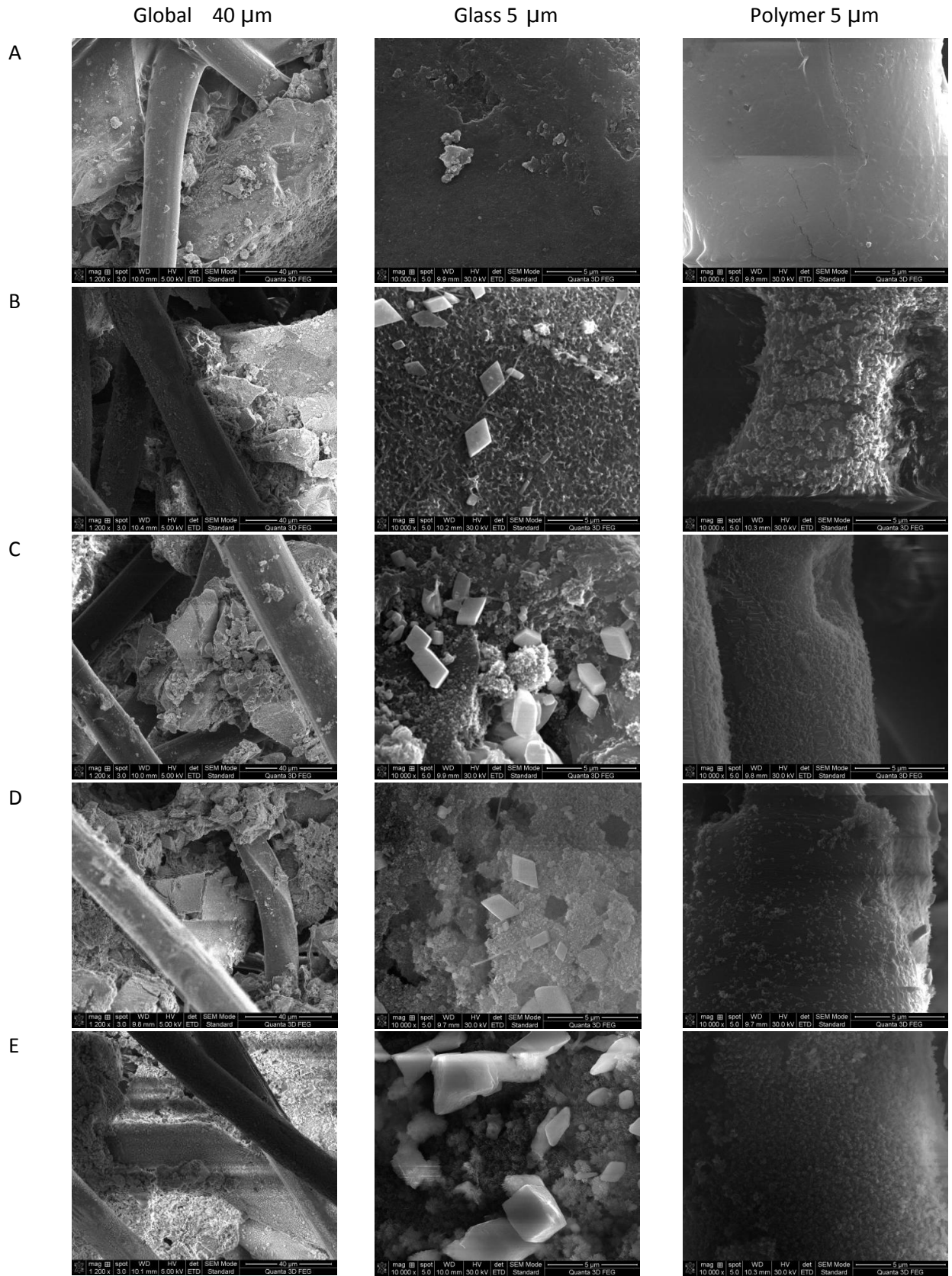
**Fig. 23** SEM images of Polymer/AgBG after incubation in SBF for : A-0, B-1, C-7, D-14, E-21, days

### 3.1.4.2 XRD

XRD results showed that characteristic HA diffraction peaks appeared after just 1 day of immersion in SBF with one peak at 26º (2θ) and another one between 2θ= 31º and 33º, as shown in Fig. 24 . The relatively narrow peaks indicate high crystalliniti of the apatite formed in vitro at this early stage of immersion in SBF. The intensity of the apatite peaks seems to increase with immersion time as shown in Fig. 4.32, suggesting the growth of the number of HA crystals formed on the PLA+PVA+BG0 composite surface. What regards the PLA+PVA+AgBG composite, one can see some additional peaks attributed to silver phosphate formation on the sample in addition to HA after SBF immersion as sown in Fig. 4.32B.
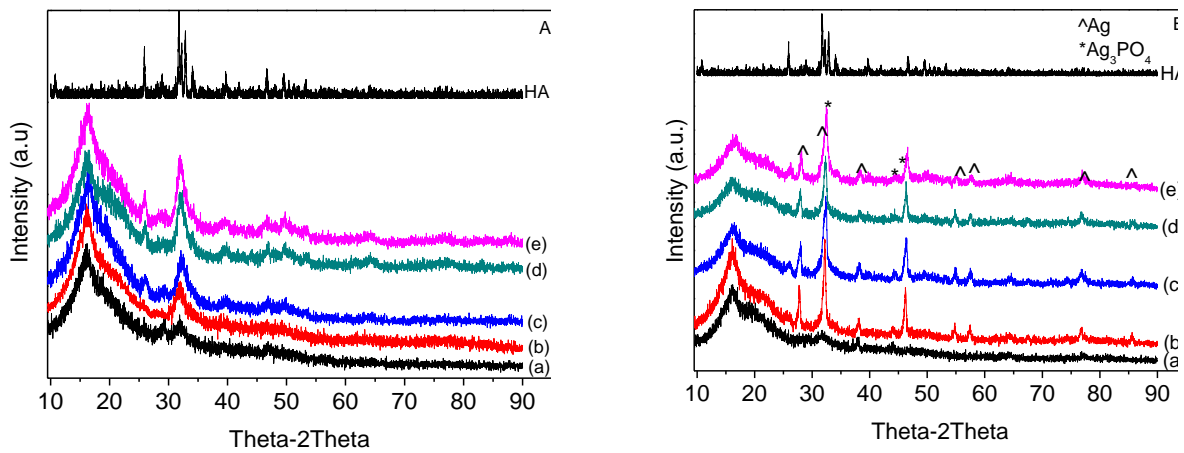


**Fig. 24** XRD patterns of the Polymer/BG) (A) and Polymer/AgBG (B) composites:
(a) prior, (b)1 day, (c) 7days, (d) 14 days (e) 21 days, of SBF soaking

### 3.1.4.3 XPS

The elemental composition recorded at the surface of the pure polymers and the composite samples before and aftere immersion in SBF was determined from XPS survey spectra (Fig. 25) and are presented in Table 5
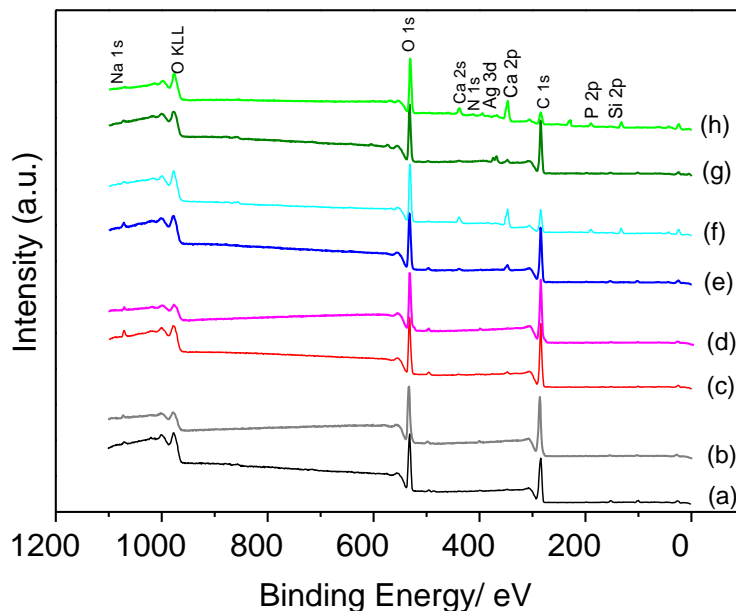
**Fig. 25** XPS survey spectra of PLA (a), PLA+PVA (c), PLA+PVA+BG0 (e), PLA+PVA+AgBG (g) before SBF soaking respectively after 21 days SBF (b), (d), (f), (h)

From the data obtained for the samples incubated in SBF, one can see that there is no HA formation on the surface of PLA and PLA+PVA samples. In the case of bioactive glass containing samples with and without silver one can observe a considerable increase of calcium and phosphorus atoms on the surface of the composites after SBF, and a decrease of the contribution given by carbon, silica and silver. This result suggest the formation of a HA layer on the surface of this composites, layer that is clearly visible also from the SEM images.

**Table 5** Surface elemental analysis results obtained from XPS survey spectra before and after incubation for 21 days in SBF

| | C | O | Si | Ca | P | Ca/P | Ag |
|---|---|---|---|---|---|---|---|
| ■ PLA | 69,429 | 27,773 | 2,798 | 0 | 0 | 0 | 0 |
| ■ PLA_SBF | 74,257 | 24,957 | 0,786 | 0 | 0 | 0 | 0 |
| ■ PLA+PVA | 74,097 | 24,554 | 0,85 | 0,499 | 0 | 0 | 0 |
| ■ PLA+PVA_SBF | 74,879 | 24,193 | 0,928 | 0 | 0 | 0 | 0 |
| ■ PLA+PVA+BG0 | 68,916 | 26,942 | 2,618 | 1,522 | 0 | 0 | 0 |
| ■ PLA+PVA+BG0_SBF | 45,467 | 39,174 | 0 | 8,1 | 7,258 | 1,116 | 0 |
| ■ PLA+PVA+agBG | 69,491 | 26,943 | 1,756 | 1,044 | 0 | 0 | 0,763 |
| ■ PLA+PVA+agBG_SBF | 32,439 | 44,79 | 1,142 | 11,273 | 9,906 | 1,138 | 0,451 |
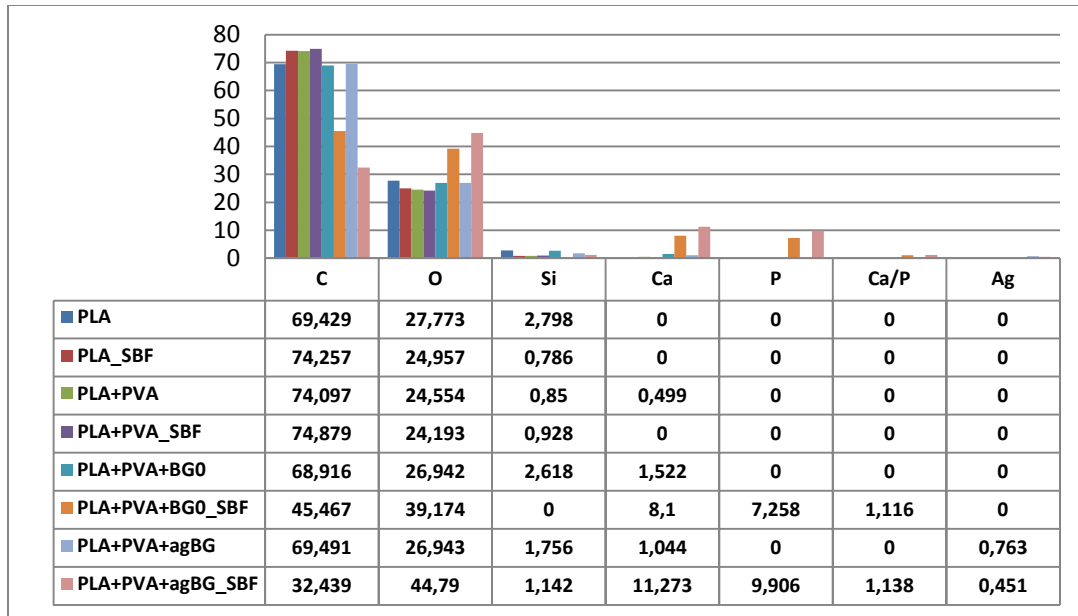
### *3.1.4.4  IR*

In Fig. 26 the FTIR-ATR of the polymer meshes with and without coating, before and after SBF immersion for 21 days are sown respectively. The spectra of the uncoated polymers (PLA and PLA+PVA) after 21 days in SBF are similar to that observed before soaking. The IR spectra of the polymers coated with both BG0 and AgBG bioactive glasses exhibit a variation in the shape of the band at 1035 cm$^{-1}$. This variation could be due to the appearance of P-O anti-symmetric stress band that is a spectral characteristic of HA.



**Fig. 26** ATR-FTIR spectra of PLA (a), PLA+PVA (c), PLA+PVA+BG0 (e), PLA+PVA+AgBG (g) before SBF soaking respectively after 21 days SBF (b), (d), (f), (h)
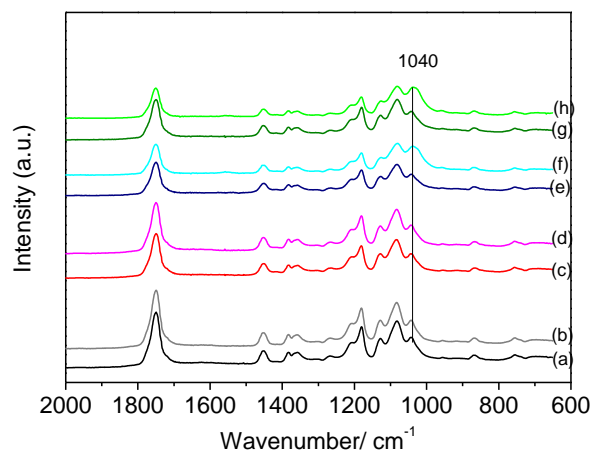
### 3.1.5  *Antibacterial effect*

Two classic pathogenic bacteria Escherichia coli, a gram positive bacteria and Staphylococcus epidermidis, a gram negative bacteria, both of them potential infection sources in wound healing, were used in the present study. The bacteria used were genetically modified light emitting bacteria, and the testing method was imaging the light emission from those bacteria in contact with the scaffolds, using a light sensitive camera. It was examined the bioluminescent time course for 24 hours of the incubated  samples together with the luminescent bacterial strains to determine the antibacterial effect.  The bioluminescence assay was performed every 2 hours in triplicates in six well plates: three control samples which are pure PLA mats and three bioactive glass containing samples. There were made a total of four plates.

As can see in Fig. 27 both bioactive glass containing composites (PLA+PVA+BG0 and PLA+PVA+AgBG respectively) inhibited the bacterial growth. The time needed for the effect varied depending on the composites. The effect also varied between bacterial species, but no significant difference was seen between gram positive and gram negative bacteria. The silver containing composite not only inhibited the bacterial growth, but it has also bactericidal effect. This affirmation is supported by the fact that the luminescent effect is proportional with the metabolism of the bacteria, so in conclusion if they do not present luminescence they don't do any metabolism and die. In the case of PLA+PVA+BG0 composite sample one can observe from Fig. 27  that the time zero is characterized by increasement in luminosity, most probably because the bacteria recognize the presence of the sample and increase their metabolism.
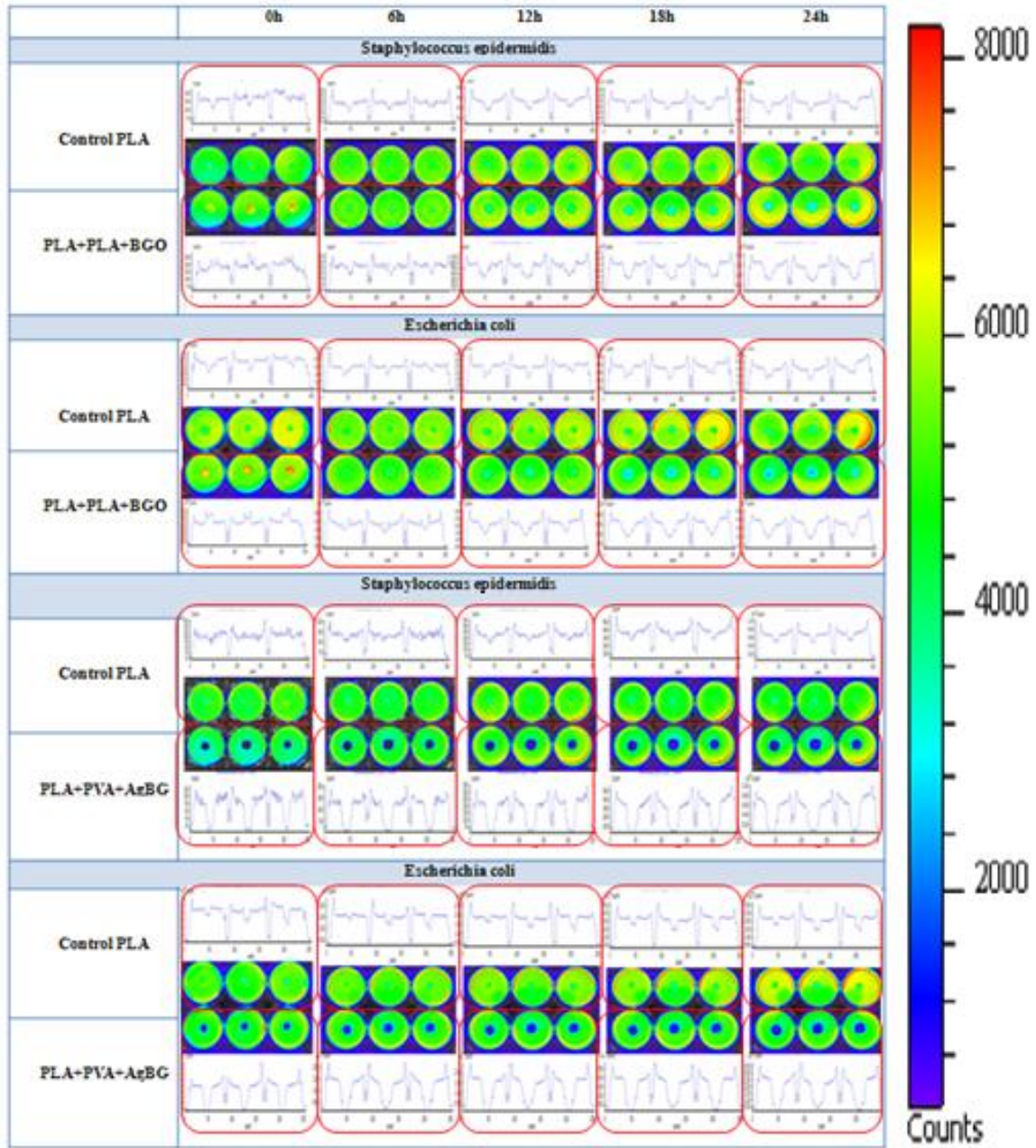
**Fig. 27** Antibacterial test results

# 4 CONCLUSIONS

- Sol-gel route has been successfully used to obtain new silicate based composites containing high silver amount

- Silver nanoparticles incorporated into the matrix, revealed by TEM and UV-vis, are potentially deposited on the pore walls and block them as seen from specific surface area and porosimetry analyses

- XRD, FTIR, SEM and XPS data reveal that the silver addition to $SiO_2$-$CaO$-$P_2O_5$ glass matrix favors the formation of HA/HCA, and also of $Ag_3PO_4$ crystals on the surface of the samples immersed in SBF

- EPR and XPS results show that high silver content incorporated in BG has an important effect in improvement of protein affinity toward this kind of materials suggesting a closer packing of proteins at the sample surface

- As expected the antibacterial properties of the bioactive glasses increased with silver concentration on both gram positive and gram negative bacteria

- Synthetic biodegradable Poly-96L/4D-lactide copolymer meshes were fabricated from the same polymer fibers

- SEM analysis revealed the porous structure of the obtained composites while the amount of bioactive glass from composites were estimated from thermal analyses

- The slurry dipping technique proved to be an apropiate technique for coating the polymers with bioactive glasses

- The high chemical reactivity of the composites was confirmed by detection of HA crystals already after first day immersion in SBF also on the polymeric phase of the composite due to dynamic SBF incubation

- The silver containing meshes exhibit a marked bacteriostatic effect on both gram negative (Escherichia coli) and gram positive (Staphylococcus epidermidis) bacteria

## General conclusion

Composite materials comprising a biodegradable polymeric phase, a bioactive inorganic phase, and an antibacterial agent were successfully obtained. These composites seem to be a promising approach for scaffold production especially regarding bone tissue engineering due to: silicate based bioactive glass that has the ability to stimulate ostegenesis and to promote bone growth: silver, a potent antibacterial agent, that forms $Ag_3PO_4$ crystals on the bioactive glass, permitting a long time release of the antibacterial agent; biodegradable and high porous polymer (PLA+PVA) that is a support for bone formation, permitting tissue ingrowths and vascularisation.

# REFERENCES

1. M. Vallet-Regi, J. Roman, S. Padilla, J.C. Doadrio, F.J. Gil Bioactivity and mechanical properties of SiO2–CaO–P2O5 glass-ceramics, J. Mater. Chem. 15 (2005) 1353-1359

2. B.S. Lee, S. H. Kang, Y.L. Wang, F.H. Lin, C.P. Lin, In Vitro Study of Dentinal Tubule Occlusion with Sol-gel DP-bioglass for Treatment of Dentin Hypersensitivity, Dent. Mat. J. 26 (2007) 52-61.

3. J.

4. S.

5. T.

6. P. A. Chrissanthopoulos, N. Bouropoulos, S.N. Yannopoulos, Vibrational spectroscopic and computational studies of sol–gel derived CaO–MgO–Si$_{O2}$ binary and ternary bioactive glasses, Vib. Spectrosc. 48 (2008) 118–125.

7. R.S. Pryce, L.L. Hench, Tailoring of bioactive glasses for the release of nitric oxide as an osteogenic stimulus, J. Mater. Chem. 14 (2004) 2303–2310.

8. T. Wenzel, J. Bosbach, F. Stietz, F. Träger, In situ determination of the shape of supported silver clusters during growth, Surface Science, 432 (1999) 257-264 + J R Osiecki, K Takusari, H Kato, A Kasuya, S Suto, The atomistic growth of silver clusters on a Si(111)7x7 surface, J. Phys.: Conference Series 61 (2007) 1107–1111

9. F.

10. R.H. Stolen, G.E. Walrafen, Water and its relation to broken bond defects in fused silica J. Chem. Phys. 64(1976) 2623-2632.

11. G. Melinte, L. Baia, V. Simon, S. Simon, Hydrogen peroxide versus water synthesis of bioglass-nanocrystalline hydroxyapatite composites, J. Mater. Sci. 2011, DOI: 10.1007/s10853-011-5700-8.

12. M.M. Pereira, A.E. Clark, L.L. Hench Effect of Texture on the Rate of Hydroxyapatite formation on Gel-Silica Surface, J. Am. Ceram. Soc. 78 (1995) 2463–2468.

13. K.S.W. Sing, D.H. Everett, R.A.W. Haul, L. Moscou, R.A. Pierotti, J. Rouquerol, et al. Reporting physisorption data for gas/solid systems, Pure Appl. Chem. 57 (1985) 603–619

14. J.R. Jones, L.M.Ehrenfried, L.L. Hench, Optimising bioactive glass scaffolds for bone tissue engineering, Biomaterials 27 (2006) 964-973

15. M.T Colomer, Nanoporous anatase thin films as fast proton-conducting materials, Adv. Mater. 18 (2006) 371–374

16. J.

17. P.

18. G. Le Saout, P. Simon, F. Fayon, A. Blin, Y. Vaills, J. Raman Spectrosc. 33, 740 (2002),

19. Mie, G., Ann.Physik, [4] 25, 377(1908)

20. M. Bellantone, H. D. Williams, and L. L. Hench, Broad-spectrum bactericidal activity of $Ag_2O$-doped bioactive glass, Antimicrobial Agents and Chemotherapy, vol. 46, no. 6, pp. 1940–1945, 2002.

21. S.

22. L.

23. Pászti Z, Petö G, Horváth ZE, Karacs A, Guczi L. Electronic structure of Ag nanoparticles deposited on Si. Solid State Commun 1998;107:329-333.

24. http://rruff.info/hydroxylapatite/display=default/R050512

25. M. Shirkhanzadeh, M. Azadegan. Formation of carbonate apatite on calcium phosphate coatings containing silver ions. J Mater Sci Mater Med 1998;9:385-391.

26. Y. Bi, S. Ouyang, J. Cao, J. Ye, Facile Synthesis of Rhombic Dodecahedral AgX/Ag3PO4 (X=Cl, Br, I) Hetero-crystals with Enhanced Photocatalytic Properties and Stabilities. Phys Chem Chem Phys 2011;13:10071-10075.

27. P. A. Kumar, M.P. Reddy, L. K. Ju, H. H. Phil, Novel Silver Loaded Hydroxyapatite Catalyst for the Selective Catalytic Reduction of $NO_x$ by Propene, Catal Lett 2008;126:78-83.

28. J.J. Buckley, A.F. Lee, L. Olivic, K. Wilson, Hydroxyapatite supported antibacterial $Ag_3PO_4$ nanoparticles. J Mater Chem 2010;20:8056-8063.

29. JK. Moffat, Spin-labelled haemoglobins: a structural interpretation of electron paramagnetic resonance spectra based on X-ray analysis. J Mol Biol 1971;55:135-146.

30. A. Simchi, E. Tamjid, F. Pishbin, A.R. Boccaccini, Recent progress in inorganic and composite coatings with bactericidal capability for orthopaedic applications. Nanomed-Nanotechnol 2011;7:22–39.

31. Q.L. Feng, J. Wu, G.Q. Chen, F.Z. Cui, T.N. Kim, J.O. Kim, A mechanistic study of the antibacterial effect of silver ions on Escherichia coli and Staphylococcus aureus. J Biomed Mater Res 2000;52:662-668.

32. A. Arvidsson, F. Currie, P. Kjellin, Y.T. Sul, V. Stenport, **Nucleation and growth of calcium phosphates in the presence of fibrinogen on titanium implants with four potentially bioactive surface preparations. An in vitro study.** J Mater Sci Mater Med 2009;20:1869-1879.

33. E. Vanea, V. Simon, XPS study of protein adsorption onto nanocrystalline aluminosilicate microparticles. Appl Surf Sci 2011;257:2346-2352.

34. L.J. Gauckler, K. Rezwan, Adsorption of biomolecules on ceramic particles and the impact on biomedical applications. Adv Sci Tech 2006;45:741-751

35. P. Ruuttila, 2000. Material properties and tissue reactions to bioabsorbable composite orbital implant, Master of Science thesis, Tampere University of Technology, Department of Materials Engineering

36. J.J.Blaker, A.R. Boccaccini, S.N. Nazhat, Thermal Characterizations of Silver-containing Bioactive Glass-coated Sutures, J Biomater Appl 1(2005) 81-98

37. B. Gupta, N. Revagade, J. Hilborn, Poly(lactic acid) fiber: An overview, Progress in Polymer Science, Volume 32, Issue 4, 2007, 455-482

38. S.S. Ray, M. Bousmina, Biodegradable polymers and their layered silicate nanocomposites in greening the 21st century materials world. Prog. Mater. Sci., 50 (2005) 962-1079.

39. D. Brizzolara, H.J. Cantow, K. Diederichs, E. Keller, A.J. Domb, Mechanism of the stereocomplex formation between enantiomeric poly(lactide)s. Macromolecules 29 (1996), 191–197

40. J.T. Yehabc, M.C. Yanga, C. J Wua, X. Wub, C.S. Wud, Study on the Crystallization Kinetic and Characterization of Poly(lactic acid) and Poly(vinyl alcohol) Blends, Polymer-Plastics Technology and Engineering, 47 (2008) Issue 12, 1289-1296

41. M. Popa, C. Vasile, I. A. Schneider Thermoxidative degradation of poly(vinyl alcohol) under dynamic thermogravimetric conditions I. Influence of heating rate and of molecular weight, J Polym Sci Part A-1: Polym Chem 10 (1972) 3679- 3684

42. C. Vasile, E.M. Călugăru, S. F. Bodonea Thermoxidative degradation of poly(vinyl alcohol) under dynamic thermogravimetric conditions. II. Influence of the hydrolysis degree J Polym Sci Polym Chem Ed 19 (1981), 897–905

43. S. P. Vijayalakshmi, Giridhar MadrasThermal Degradation of Water Soluble Polymers and Their Binary Blends, Journal of Applied Polymer Science, 101 (2006) 233 – 240

44. Z. Zhoua, X. Liua, Fabrication of Poly-l-lactide Biomaterials with High Mechanical Properties Using Fiber Oriented Pressing, Journal of Macromolecular Science, Part B 47 (2008) 847-858

45. E. Pamula, M. Blazewicz, C. Paluszkiewicz, P. Dobrzynski, FTIR study of degradation products of aliphatic polyesters-carbon fibres composites, Journal of Molecular Structure, 596 (2001), 69-75

46. P. Ping, W. Wang, X. Chen, X. Jing, Poly(epsilon-caprolactone) polyurethane and its shape-memory property, Biomacromolecules 6 (2005) 587-92.

47. J.W. Huang, Y.C. Hung, Y.L. Wen, C.C. Kang, M.Y. Yeh, Polylactide/Nano and Microscale Silica Composite Films.I. Preparation and Characterization, Journal Of Applied Polymer Science, 112 (2009), 1688 – 1694

48. Elizabeth Fonseca dos et al. Synthesis and characterization of poly (vinyl alcohol) hydrogels and hybrids for rMPB70 protein adsorption. Mat. Res 9 (2006), 185-191

49. J. Olsen-Claire, J. J. Blaker, J. A. Roether, A. R. Boccaccini, G. Schmack, K. Gliesche, Bioglass® Coatings on Biodegradable Poly(3-hydroxybutyrate) (P3HB) Meshes for Tissue Engineering Scaffolds, Materialwissenschaft und Werkstofftechnik 37 (2006) 577–583